8-2011

Numerical simulation of the aerodynamic performance of an H-rotor.

Yan Chen
University of Louisville

Recommended Citation

Chen, Yan, "Numerical simulation of the aerodynamic performance of an H-rotor." (2011). *Electronic Theses and Dissertations.* Paper 237.
https://doi.org/10.18297/etd/237

NUMERICAL SIMULATION OF THE AERODYNAMIC PERFORMANCE OF AN H-ROTOR

By

Yan Chen

B.S., North China University of Water Conservancy and Electric Power, 2009

China

A Thesis

Submitted to the Faculty of the

J.B. Speed School of Engineering of the University of Louisville

in Partial Fulfillment of the Requirements

for the Degree of

Master of Science

Department of Mechanical Engineering

University of Louisville

Louisville, Kentucky

August 2011

NUMERICAL SIMULATION OF THE AERODYNAMIC PERFORMANCE OF AN H-ROTOR

Submitted by: _____ Yan Chen _____

Yan Chen

A Thesis Approved On

_____ August 1st, 2011 _____

(Date)

By the Following Thesis Committee:

_____

Dr. Yongsheng Lian, Thesis Director

_____

Dr. Ellen G. Brehob

_____

Dr. R. Eric Berson

ii

ACKNOWLEDGEMENTS

I would like to thank my advisor Dr. Yongsheng Lian for giving me the opportunity to work in the Computational Fluid Dynamics Laboratory, guiding me in learning CFD process and supporting me in preparing this thesis.

ABSTRACT

NUMERICAL SIMULATION OF THE AERODYNAMIC

PERFORMANCE OF AN H-ROTOR

Yan Chen

August 1st, 2011

Vertical axis wind turbines (VAWTs) are devices to convert wind energy into electricity. Unlike horizontal axis wind turbines (HAWT) where the main rotor shaft is set horizontally, VAWTs use vertical rotor shaft. Unlike HAWTs, VAWTs can be effectively used in urban environment where flow is characterized with unsteadiness and turbulence. The efficiency of the VAWTs highly depends on the aerodynamics of the wind blades. In this thesis we study the aerodynamics of the H-rotor, one type of VAWTs using computational fluid dynamics methods. Two different approaches are used in this study. One is based on direct numerical simulation (DNS) method and another is based on Reynolds averaged Navier-Stoke (RANS) model. For DNS study we solve the incompressible Navier-Stokes equations with a CFD package, OVERTURE. An overlapping moving grids technique is employed to handle the rotation of the wind turbine. For RANS simulation we used a commercial CFD package ANSYS-Fluent. The

sliding mesh model of ANSYS-Fluent is applied to evaluate unsteady interaction between the stationary and rotating components.

Our simulation shows that the DNS cannot correctly predict the power coefficient due to the lack of grid resolution at high Reynolds numbers. The RANS simulation results closely match the experimental data and RANS provides a way to study wind turbine aerodynamics in an efficient and reliable manner. Our simulation shows that the rotor with NACA0015 blade section obtains a maximum power coefficient of 0.16 at tip speed ratio of 2.5 for mean wind velocity of 3.9m/s. By replacing the blade section with NACA0022 airfoil profile, the maximum power coefficient of the rotor can be improved to 0.21 at tip speed ratio of 2.5 in the same wind conditions.

TABLE OF CONTENTS

LIST OF TABLES

LIST OF FIGURES

I   INTRODUCTION

In the 21th century, due to the energy crisis, wind power generation has experienced a tremendous growth with the advancement of new techniques and has been considered as an environmentally friendly and economically competitive means of energy resource. By the end of 2010, all installed wind turbines generated 430 terawatthours per year, equaling 2.5% of the global electricity consumption (WWEA, 2010).

H-rotor, a vertical axis wind turbine (VAWT), is suitable for urban areas because it has relatively high power efficiency and is not sensitive to turbulence. In this thesis, we will study the aerodynamic performance of H-rotor using computational fluid dynamics techniques. Two different analysis tools are used for that purpose. One is an in-house code and another is commercial software.

A. Background

The following sections summarize the history of wind energy conversion system and the current research and future trends. Horizontal axis wind turbines (HAWTs) and VAWTs are compared. Different analysis tools for wind turbine study are also illustrated.

1. Wind energy conversion system

Since early 1990s, worldwide development of wind energy expanded rapidly. It was reported that worldwide capacity of wind energy has reached 196,630 MW, an increase from 158,988 MW in 2009 (WWEA, 2010). Although there is a lack of political support for wind energy utilization, the overall size of new wind turbine is 37,642 MW in 2010, just a little less than the peak size 38,312 MW in 2009.

The wind energy conversion system (WECS) is a machine that can convert kinetic energy of the wind into electricity or other forms of energy. The major components of WECS include wind turbine, electricity generator, interconnection apparatus and control system. The wind turbine plays a role as an energy extractor and it will determine the efficiency of system at the beginning of the process. In 1896, Poul la Cour, a Danish scientists applied modern fluid dynamics theory to study the aerodynamic performance of windmills. Since then, modern wind turbine development has been based on aerodynamic theory and wind tunnel experiments which supply great tools to design wind turbine and improve their aerodynamic performance (Krohn, 2002).

2. History of wind turbine

Wind energy has been utilized as an energy source for a long time. The earliest practical windmills are Persian vertical-axis windmill in Sistan, A.D. 1300 and Chinese vertical-axis windmill, A.D. 1219 for grain-grinding and water pumping (Shepherd, 2009). During the Middle Ages, horizontal axis windmills were built in Europe for the same tasks. The first attempt to generate electricity by a horizontal axis wind turbine was

made by Scottish academic, James Blyth in 1887. Later, American inventor Charles F. Brush built the first automatically operated wind turbine for electricity production.

Modern wind turbines can be categorized into two basic groups based on their rotation axis: the horizontal-axis variety, and the vertical-axis design. The great majority of wind turbines in the world are aerodynamically improved versions of traditional horizontal axis wind turbine. The rotor is similar to a propeller but the action is different. A propeller delivers forward thrust at the expense of torsion of the propeller axis, while a wind turbine delivers torque to the generator shaft from incoming wind. Relying on aerodynamic lift, modern HAWTs produce higher rates of power than those wind turbines relying on drag to generate power (Paraschivoiu, 2002). The power conversion efficiencies for HAWTs range from 40% to 50% (Muljadi, 1989).

During the 20th century HAWTs continued to evolve. As a result, large and advanced HAWTs came out. Over the past decades the performance of HAWTs has increased considerably due to improved airfoils, variable speed or multi-speed operation and more efficient drive trains. Recently VAWTs have drawn attention due to the advantage of generating power at smaller scales.

3. Comparison of HAWTs and VAWTs

There are mainly three kinds of VAWTs; Savonius, Darrieus, and H-rotor. Figure I-1 shows a common horizontal axis wind turbine and three kinds of vertical axis wind turbines. The Savonius rotor has an "S-shaped" cross-section with a vertical cylinder sliced in half from top to bottom (Paraschivoiu, 2002). The Darrieus rotor was patented by the U.S. Patent office in the name of G. J. M. Darrieus in 1931. The patent states that

the blades "have a streamline outline curved in the form of skipping rope" (Darrieus, 1931). The Darrieus rotor has curved blades that approximate the shape of a perfectly flexible cable, of uniform density and cross section hanging freely from two fixed points under the action of centripetal forces. Such a shape minimizes inherent bending stresses.
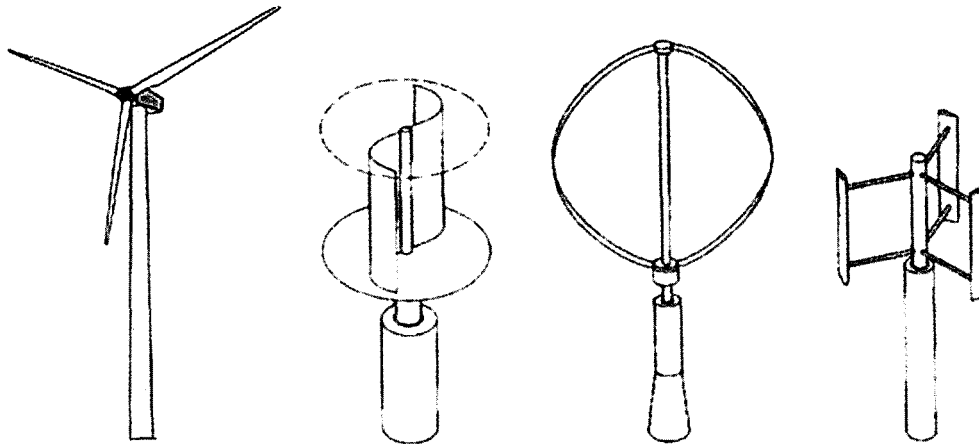
Figure I-1 HAWT, Savonius, Darrieus and H-rotor

The main advantage of VAWTs is their ability to receive wind from any direction (Eriksson, 2006). Compared to VAWTs, HAWTs rely on a yaw system to keep it facing the wind direction. The yaw system is costly and could fail during operation. The entire yaw system, rotors, gearbox and generator are installed on the top of the tower for HAWTs; while VAWTs allow heavy machineries to be located at the bottom of the tower. Compared with HAWTs, the installation, operation and maintenance of VAWTs are much easier. Furthermore, by applying direct drive generator VAWTs can eliminate the energy loss from gearboxes. The overall advantages of VAWTs make them more convenient for maintenance, particularly on large units or when operating in potential icing conditions (Eriksson, 2008).

4

Because the power output is proportional to the size squared of the wind turbine, increasing the size of the wind turbine can significantly increases the power generation. Increasing the size of the turbines is a trend in wind turbine development. Figure I-2 shows the progression of HAWT size over last two decades. However, as the blade size increases, the blade mass expands at the rate of the cubic of blade length. The HAWT's blade is subject to gravity-induced reversing stress at the root of the blades (Morcos, 1996), which is believed to be the main limitation for increasing the size for HAWTs. Furthermore, the performance of HAWTs is negatively affected by the turbulence in the wind. Riegler points that VAWTs can enjoy the high wind gusts which are the best atmosphere for wind generation. In the urban and mountainous areas VAWTs can be used in lieu of HAWT designs (Riegler, 2003).
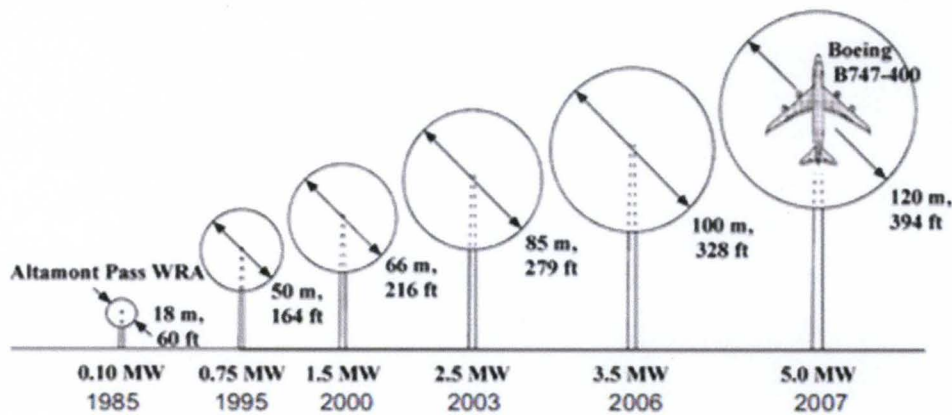
Figure I-2 HAWT size to power relationship (van Dam, 2009)

Figure I-3 plots power coefficient (C_P) versus tip speed ratio (λ) for three different turbines. The power coefficient is the parameter to calibrate efficiency of the turbine representing the portion of energy that wind turbine extracts from the wind. The tip speed ratio is the ratio of the blade tip velocity to free stream velocity. As a drag-type device,

the maximum power coefficient of the Savonius rotor which is not included in Figure I-3 is 0.3, which is much lower than modern HAWTs. In the real world the wind turbine often operates at the rotating speed around the maximum power coefficient. Although HAWTs perform slightly better than VAWTs, the conveniences of VAWTs provide the reason for VAWTs for their utilization. Besides, since no wind turbines can operate beyond the theoretical Betz limit of 0.59 (Betz, 1966) there won't be much great improvement in turbine efficiency. In addition, the optimum tip speed often represents the noise level from the turbine, the higher the tip speed the higher the noise level will be. Iida predicts that the noise level of VAWTs is about 70dB, 10dB lower than HAWTs (Iida, 2004).
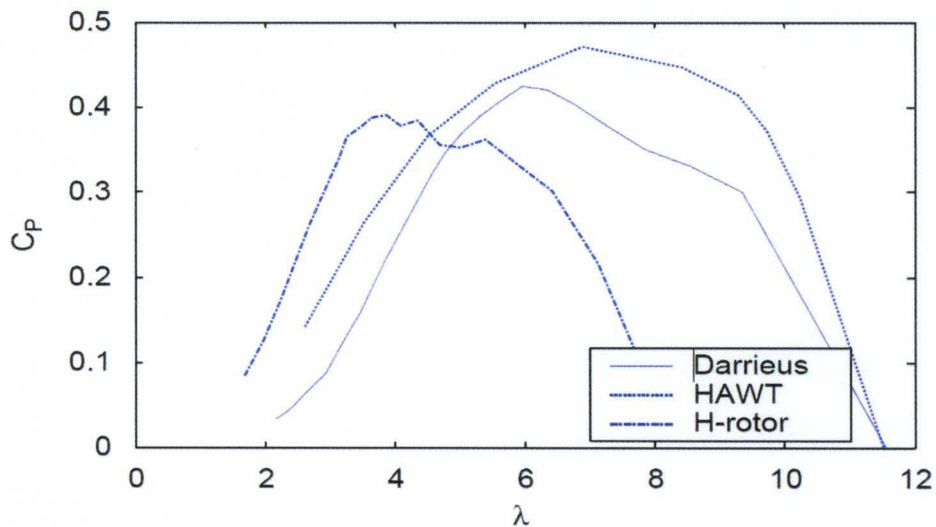
Figure I-3 Power curves for the HAWT, the Darrieus and the H-rotor (Eriksson, S., Bernhoff, H., and Leijo, M., 2006)

B. Aerodynamic rationale

The prototype of the H-rotor is presented in Figure I-4. The H-rotor is constituted by several straight blades with airfoil cross section which are the main power generating structure. The strut and supporting arms serve as structural support. The H-rotor blades generate lift and drag forces by the motion of spinning in the wind and torque is produced by the force in the tangential direction. Therefore, the power is generated by the H-rotor. A two dimensional simulation is carried out to estimate the aerodynamic performance of H-rotors. Though the H-rotor has a simple appearance, its aerodynamic performance is complex during the rotation. The general geometrical and aerodynamic features are presented here.
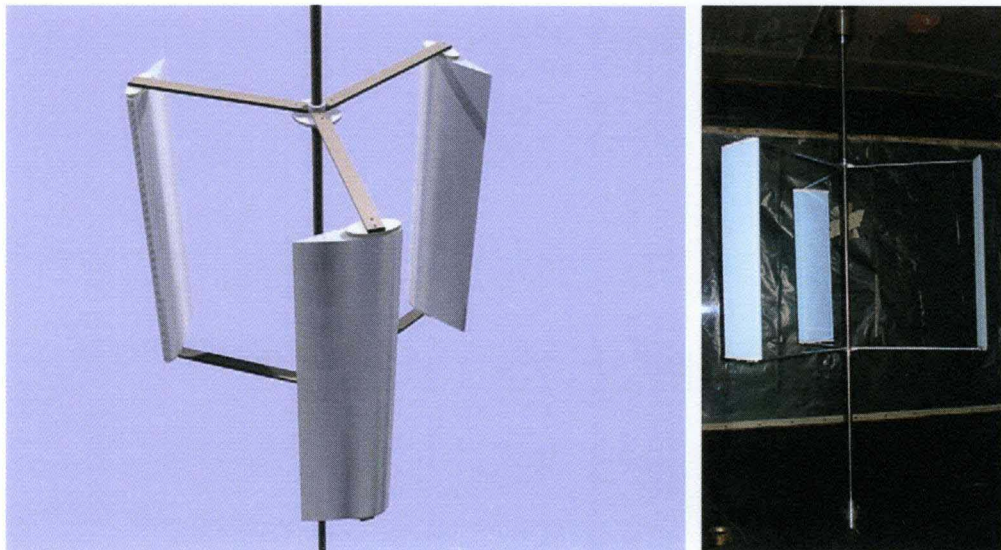
**Figure I-4 CAD model of the turbine model and model turbine in the wind tunnel
(Howell, 2010)**

1. Aerodynamic features of H-rotors

As mentioned before, the forces generated from wind can produce power. Figure I-5 shows the directions of the lift and drag and their normal and tangential components. As fluid flow flows past the surface of a body, a surface force will be exerted on it. Lift is the component of this force that is perpendicular to the oncoming flow direction. In contrasts to the lift force, the drag is the component of the surface force parallel to the flow direction. In aerodynamics, the lift and drag forces are commonly carried to analyze the aerodynamic characteristics of an airfoil. On a rotating H-rotor, the forces can be also expressed in tangential and normal directions. The tangential force can be obtained by the difference between the tangential component of lift and drag forces and the normal force perpendicular to the rotating direction is the difference between their normal components. The tangential force F_t and the normal force F_n can be expressed as below:

$$F_t = Lsin\alpha - Dcos\alpha \tag{1.1}$$

$$F_n = Lcos\alpha - Dsin\alpha \tag{1.2}$$

The force coefficients can be expressed as:

$$C_L = \frac{L}{1/2\rho c V_\infty{}^2} \tag{1.3}$$

$$C_D = \frac{D}{1/2\rho c V_\infty{}^2} \tag{1.4}$$

$$C_t = \frac{F_t}{1/2\rho c V_\infty{}^2} \tag{1.5}$$

$$C_n = \frac{F_n}{1/2\rho c V_\infty{}^2} \tag{1.6}$$

In Figure I-5, W, the relative velocity, is equal to the vector sum of freestream velocity and rotating velocity. And α is the angle of attack. θ ($\theta < 360^o$) is the azimuth

8

angle of the blade and the beginning position is facing against the freestream velocity direction.
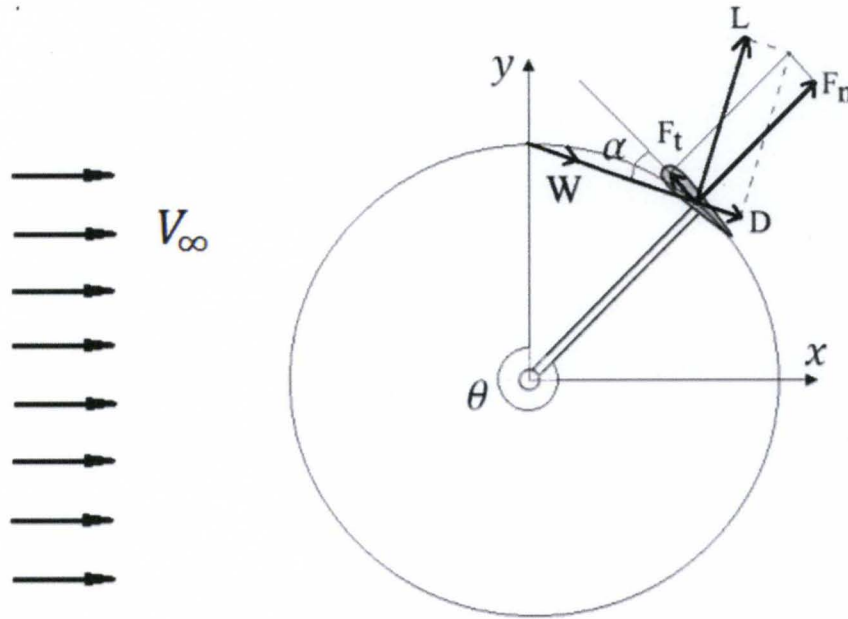
Figure I-5 Force diagram of a blade airfoil

Due to the angle of attack and relative wind speed changes with the azimuth positions, the forces vary and can be considered as a function of azimuth angle. The relative wind speed can be obtained by the vector sum of inlet wind velocity and rotating velocity. The AOA is the angle between relative wind velocity and the blade rotating direction. Figure I-6 presents the changing relative wind velocity and AOA in one rotating cycle. At different TSRs, due to the change of the AOA and the relative wind speed the blade exhibits various aerodynamic performance in one cycle. The AOA range is determined by the TSR. Figure I-7 plots AOA versus azimuth angle at different tip speed ratios. The range of AOA at low TSR is larger than that of high TSR. When the TSR increases, the rotating velocity will become dominant in the relative wind speed.

9

The AOA won't show much change when increasing the TSR. The relation between the AOA and TSR is expressed in Equation (1.7).

$$\alpha = tan^{-1} \frac{sin\theta}{cos\theta + \lambda} \qquad (1.7)$$

where θ is the azimuth angle and λ is the TSR. At different TSRs, both angle of attack and relative wind speed are changing. At high tip speed ratios, the rotating speed is so high that the freestream velocity could be neglected.
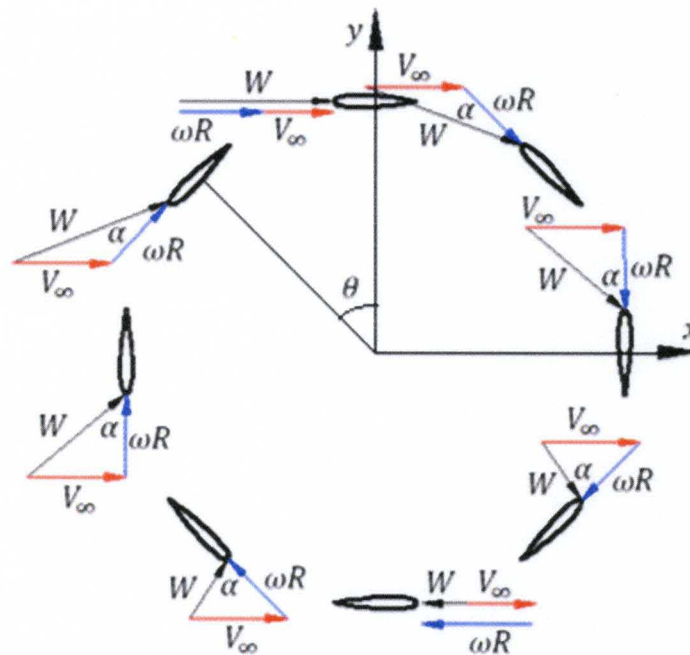
Figure I-6 AOA (α) and relative wind speed at various azimuthal position

10
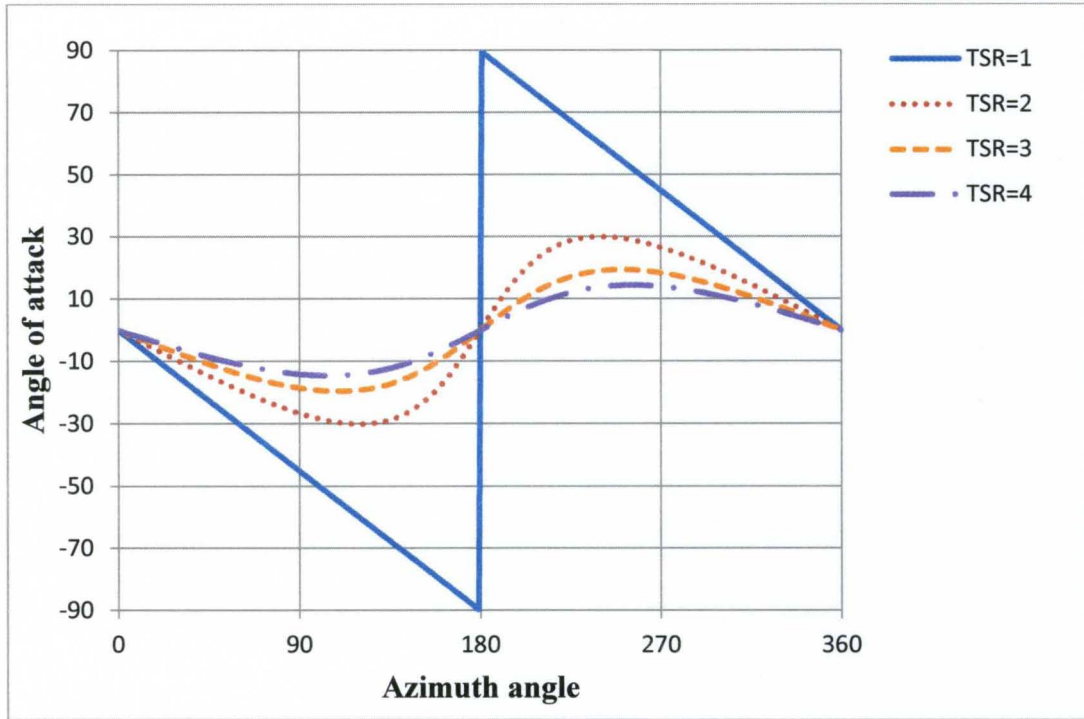
Figure I-7 The angle of attack versus the azimuth angle at different TSRs

The averaged tangential force (F_{ta}) can be obtained.

$$F_{ta} = \frac{1}{2\pi} \int_0^{2\pi} F_t(\theta) d\theta \qquad (1.8)$$

The torque (T) is generated by the tangential force. The torque can be expressed.

$$T = NF_{ta}R \qquad (1.9)$$

where N is the number of blades and R is the radius of turbine. And the torque coefficient can be expressed as:

$$C_T = \frac{T}{1/2\rho R A V_\infty{}^2} \qquad (1.10)$$

where A is the cross-sectional area of the wind turbine. In 2D simulation,

$$A = 2R \qquad (1.11)$$

The total power (P) obtained can be expressed.

11

$$P = T \cdot \omega \qquad\qquad (1.12)$$

where T is the generated torque and ω is the angular velocity.
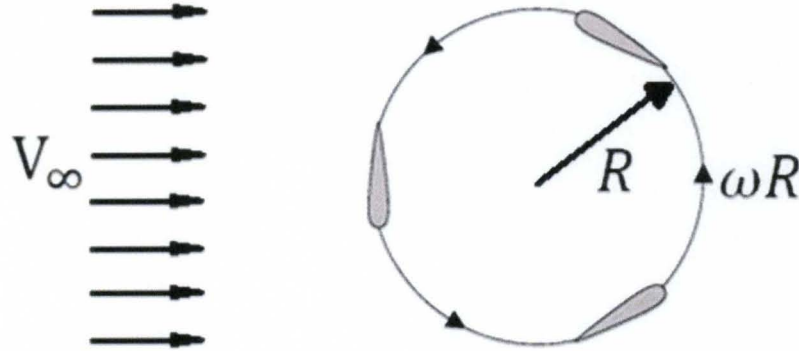
Figure I-8 The two dimensional model of the H-rotor

Figure I-8 shows the wind direction and rotation direction of a two dimensional model of H-rotor. The wind direction is perpendicular to the turbine rotating axis. The strut and supporting arms are neglected in the 2D simulation for geometrical simplicity. The general geometric features of H-rotors are rotor radius (R), blade length (H), number of blades (N), chord length (c) and airfoil shape. These features are all determinants to the aerodynamic performance of the rotor. And the environmental conditions that the rotor is operating in would affect the performance. These conditions include wind speed (V_∞), air viscosity (μ) and air density (ρ). And also the angular rotating speed (ω) of the H-rotor could affect its own performance. Usually, the performance of an H-rotor is evaluated by the power coefficient. The power coefficient is defined as the ratio of the power that the turbine can extract from the wind energy.

The power in an air stream available to a downstream wind turbine is proportional to the cross-sectional area (A) of the wind turbine normal to stream, and also proportional to the cubic mean wind speed (V_∞). Therefore, the available wind power (P_W) can expressed.

$$P_W = \frac{1}{2}\rho A V_\infty^3 \tag{1.13}$$

The power coefficient (C_P) is given in equation (1.12):

$$C_P = \frac{P}{P_W} \tag{1.14}$$

Based on the determinants of the rotor performance, the power coefficient can be expressed as a function of rotation speed, free stream velocity, chord length, rotor radius, blade length, fluid viscosity, density, and blade number.

$$P = f(\omega, V_\infty, c, R, H, \mu, \rho, N) \tag{1.15}$$

By doing dimensionless analysis, the power coefficient can be expressed as:

$$C_P = \Phi(\frac{\omega R}{V_\infty}, \frac{c}{R}, \frac{H}{R}, \frac{\mu}{\rho V_\infty R}, N) \tag{1.16}$$

The nondimensional parameters in equation (1.15) are defined as below. The ratio between the blade tip speed and the wind speed is defined as the tip speed ratio (TSR):

$$\lambda = \frac{\omega R}{V_\infty} \tag{1.17}$$

The solidity of the turbine

$$\sigma = \frac{c}{R} \tag{1.18}$$

When the solidity of the turbine is determined, the other parameters are commonly defined by the chord length of airfoil.

The aspect ratio

13

$$a = \frac{H}{c} \qquad\qquad (1.19)$$

The Reynolds number

$$Re = \frac{\rho V_\infty c}{\mu} \qquad\qquad (1.20)$$

All these nondimensional parameters are necessary to be considered in designing H-rotor. In the design process the airfoil shape is also another important factor in determining the H-rotor's performance. Including the airfoil shape, these nondimensional parameters have been widely used in optimization of the wind turbines.

2. Blade element momentum theory

One of the most important methods in wind turbine research is the classical Blade Element Momentum theory (BEM) which was first introduced by Glauert. The theory is based on one dimensional momentum theory in which forces are defined as distributing continuously in the azimuth direction. The rotor is considered as an ideal permeable disc. Thereby, it is frictionless and there is no rotational speed is in the wake. The flow is assumed to be steady and incompressible. A control volume including the rotor is separated in the fluid area. Figure I-9 shows the velocity distribution in the control volume. The rotor acts as a drag device slowing the wind speed from V_∞ far upstream of the rotor to V at the rotor plane and to V_1 in the wake.

Close upstream of the rotor there is a small pressure rising from p_0 to p before a discontinuous pressure drop Δp over the rotor. The pressure recovers back to p_0 downstream of the rotor. The conservation of mass and conservation of momentum are applied to the control volume.
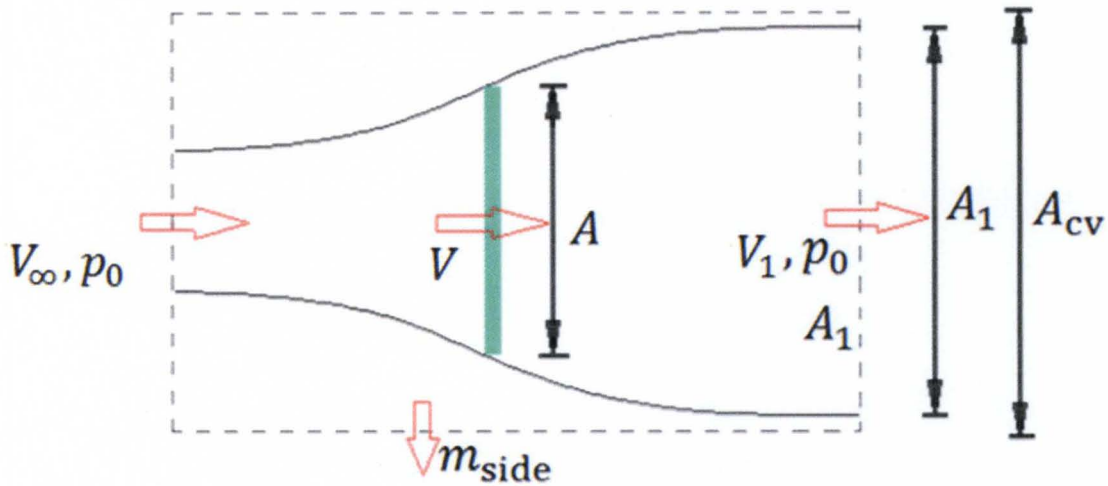
Figure I-9 Illustration of velocities and pressures upstream and downstream of the rotor

The induced velocity, V, and induced factor, a, can be obtained from the equations given below.

$$V = \frac{1}{2}(V_\infty + V_1) \tag{1.25}$$

$$a = 1 - \frac{V}{V_\infty} \tag{1.26}$$

For most streamtube models, the induced velocity is a critical parameter. If the induced velocity is obtained, then the torque and power coefficient could be calculated. The power coefficient can be expressed.

$$P = FV = 2\rho V_\infty{}^3 a(1-a)^2 A \tag{1.27}$$

$$C_P = \frac{P}{\frac{1}{2}\rho A V_\infty{}^3} = 4a(1-a)^2 \tag{1.28}$$

The equation is shown graphically in Figure I-10. The maximum power coefficient (Betz limit) 16/27 is obtained when a equals to 1/3 that means the portion that the turbine can extract wind could not be more than 16/27.

15
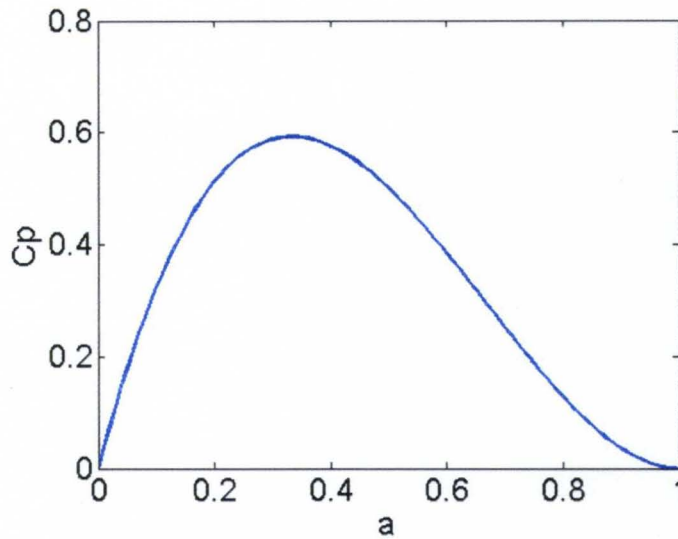
Figure I-10 The power coefficient as a function of induced factor

C. Literature review

Various models were applied to study the aerodynamic performance of H-rotors. Earlier, when the computational source wasn't enough to study a complex problem, such as the flow around the H-rotors, empirical aerodynamic models were developed based on data from wind tunnel experiments. These models were improved when more data was available. Today the empirical models are still used on the research. At the same time, with the development of computers and algorithms, computational fluid dynamics (CFD) is also applied on the research of H-rotors.

1. Aerodynamic models for H-rotor

Templin (1974) first introduced the single streamtube model (Figure I-11) based on blade element momentum theory which was combined blade element and momentum theory together. The momentum theory was applied on the streamtube. The blade element

theory was to examine the forces generated by the airfoil lift and drag coefficients at various sections. It's the simplest model to predict performance of Darrieus-type VAWTs. The entire turbine was assumed to be enclosed within a single streamtube in this model. The induced velocity was considered as a constant and can be obtained by equating the streamwise drag with the change in axial momentum. The effects of geometric variables, zero-lift-drag coefficient and airfoil stall on the performance were included in the analysis. Noll (1980) added the turbulent wake state, dynamic stall and strut drag to their single streamtube model.
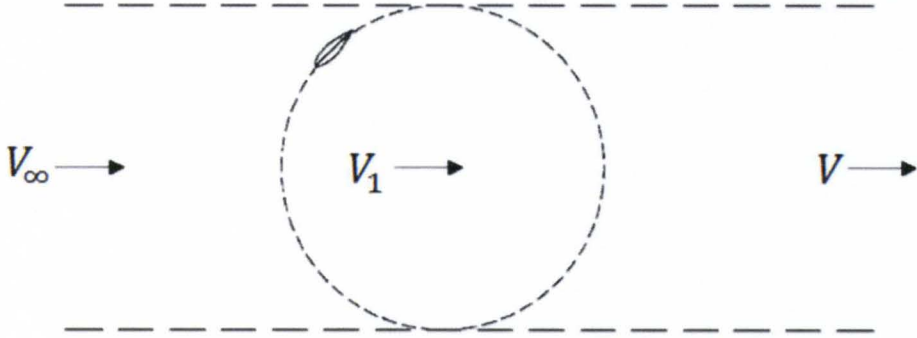
Figure I-11 Single streamtube model
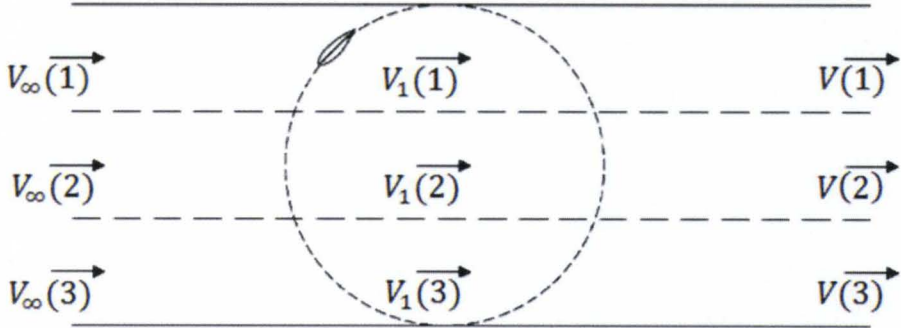
Figure I-12 Multiple streamtube model

In 1974, Wilson and Lissaman proposed an improved streamtube model, the multiple streamtube model (Wilson, 1974). The swept area of the turbine was divided into several parallel streamtubes as shown in Figure I-12. In this model the blade element momentum theory was applied. As the flow was considered as inviscid, only lift force was required to calculate the induced velocity. The theoretical lift was considered in the calculation. The velocity varied in both vertical and horizontal directions. However, this model could be only applied for high rotating speed wind turbine. The theoretical lift force was expressed as:

$$C_L = 2\pi sin\alpha \hspace{4cm} (1.29)$$

Later, Strickland (1976) proposed another multiple streamtube model for Darrieus type VAWT. In this model, the induced velocity was calculated by equating the forces including drag to momentum change along streamtubes. The experimental airfoil data were used as forces in calculation (Klimas, 1985). The sources of the forces used in the two multiple streamtube models were different from each other. The latter one has the capability of examining different types of airfoils at different Reynolds number. However, this model gave slow convergence as a result of complicacy.

Paraschivoiu (1981) presented a double multiple streamtube model (DMSM) to predict the performance of Darrieus wind turbine. In this model the upstream and downstream half cycles of the turbine were calculated separately. Therefore, the streamtube induced velocity was calculated for both upstream and downstream. The double multiple streamtube model gave a better prediction of the performance. In 1983, Paraschivoiu improved the double multiple streamtube model by considering the induced velocity variation as a function of azimuth angle. The secondary effects including blade

18

geometry, the rotating tower, and aerodynamic spoiler for the wind turbines were considered in this mode (Paraschivoiu, 1983). But this model overpredicted power when the wind turbine conserved high solidity. Some convergence problems happened at high tip speed ratios. Paraschivoiu (1988) improved his double multiple streamtube model by considering dynamic stall. Although the enhanced model improved the accuracy of original model, large discrepancy still existed compared with experimental data.

Vortex models were also used to predict the H-rotor performance. The vortex models were potential flow models in which the velocity field was calculated by the influence of vorticity in the wake of the blades (Strickland, 1979). The induced velocity can be related to filament strength by the Biot-Savart's law. Vortex model can be divided into two types: prescribed wake models and free wake models (Strickland, 1981). Today, vortex models have been modified by adding dynamic stall effects. Although vortex model took more computational time than streamtube model, it still relied on significant simplifications (Wilson, 1980).

2. CFD models

Due to the complexity of the unsteady aerodynamics of the H-rotor, CFD methods become an attractive way to analyze the aerodynamic performance. Compared with other models, CFD methods are more direct and general. The fluid field captured around the wind turbine will provide great data for analysis. Also from the unsteady state model, the flow characteristics can be obtained instantaneously.

Allet and Paraschivoiu (1995) discretized steady, incompressible Navier-Stokes equation in cylindrical coordinates by the control volume approach. The CFD results

were compared with the DMSM results and experimental data. As the dynamic stall effects were added in both models, both CFD simulation and DMSM simulation can predict the power coefficient accurately at low tip speed ratio where the dynamic stall happened. However, when it came to instantaneous data, CFD simulation offered a much better prediction. For the higher tip speed ratios, CFD simulation also presented better performance than DMSM simulation (Allet and Paraschivoiu, 1995).

Mertens studied the performance of H-rotors in skewed flow by DMSM simulation (2003). The CFD technique was applied to calculate the turbulent separation over a rectangular model building. The skewed angle of wind velocity vector from CFD modeling was considered in the DMSM simulation of aerodynamic performance. The modeling results showed an increase of the power coefficient when H-rotor was in skewed flow. This has also been validated by wind tunnel experiments. In addition, the power coefficient of H-rotors increased more at high aspect ratio than that at low aspect ratio while the HAWT showed a decrease in skewed flow. VAWTs are more favorable for operation on top of a roof, where the wind vector is not horizontal.

In 2005, Horiuchi *et al.* examined the applicability of CFD to wind turbine. The detached eddy simulation (DES) was employed for numerical simulation. They found the numerical simulation was applicable to the flow analysis for H-rotors. The phenomenon that the wind velocity could not recover in x/r=10 downstream need to be considered when installing wind turbine in large quantity. (Horiuchi, Ushiyama, and Seki, 2005)

Guerri (2007) investigated the aerodynamic performance of a small rotating vertical axis wind turbine by using a RANS solver and moving meshing technique. The SST k-omega model was applied to the two dimensional simulation. Blade forces and

torques obtained from integrating the pressure and shear stress over the blade surface were compared with a multiple streamtube model results. The dynamic stall phenomenon was captured by the CFD model. Besides, it was found that the rotational speeds predicted by CFD model were less than those by the multiple streamtube theory. The modeling results showed that the CFD technique gave a good evaluation of wind turbine performances and remained sensitive to the airfoil section data. Also, moving meshing which was handling the rotation of the wind turbine was reliable in computation of the blade forces (Guerri, Sakout and Bouhadel, 2007).

Ferreira (2007) simulated the dynamic stall of the H-rotor by CFD models and validated the stalls with Particle Image Velocimetry data. A two-dimensional model was created representing the middle section of the H-rotor. Two different turbulence models were adopted in the paper. RANS simulation, LES simulation and DES simulation gave a fairly accurate prediction of the loads on the blades. Compared to RANS results, the LES force curve presented the unsteadiness of the forces caused by the small vortex shedding which cannot be captured by the RANS model. When it came to modeling vortex shedding, the DES simulation matches the PIV data because it can better resolve the separated flows. However, DES required more computational resources and long computational time (Iida, 2004). DES was also adopted by Iida, but it was only used to understand the flow structures and validate the simulation. The vortex method was applied to estimate the performance and aerodynamic noise of wind turbines. The complicated wake can be captured and a reasonable power coefficient is obtained by the vortex method.

Hamada (2008) studied both two-dimensional and three-dimensional H-rotor with RNG k-epsilon turbulence model. The 2D unsteady simulation showed that negative torque is generated at azimuth angle $\theta = 0$ degree and reached the minimum value of torque at $\theta = 13$ degrees. After $\theta = 13$ degrees, torque increased as lift direction became more favorable for positive torque contribution. Also more lift was generated as a result of the angle of attack increasing. At $\theta = 90$ degrees, positive torque reached the maximum value. After then, the torque decreased as the drag increased until dynamic stall happened. At $\theta = 180$ degrees, the torque reached a negative value again as a result of drag becoming dominant. In the downwind direction, a smaller positive torque was generated. As the variation in both the direction and the magnitude of the relative velocity vector the dynamic stall behavior of the VAWT blade was different from that of a pitching airfoil. Compared with two dimensional model, the three dimensional CFD model could capture blade tip vortices and supporting arm drag. As a result, the three dimensional CFD model of wind turbine performed a significant decrease of power coefficient (Hamada, 2008).

Design optimization on H-rotor has also been conducted based on CFD analysis tools. Staelens, Saeed and Paraschivoiu (2003) presented an improved performance of H-rotor by varying the blades' pitches. Their aerodynamic code based on Double Multiple Streamtube Model was used to simulate the cases of three different modifications. In the first modification model, the local angle of attack was kept below the stall value throughout the whole rotation period. In the second modification, the stall angle would replace the local angle of attack when the local angle of attack exceeded the static-stall angle. In the last modification, a sinusoidal correction function was added to correct the

local angle of attack. The results showed that all the modifications could increase the wind turbine performance significantly. However, the first case required sharp jumps in the local angle of attack which was impossible to realize mechanically. For the second case, though the jumps in local angle of attack were eliminated, the correction function of local angle of attack was discontinuous which may result in an early fatigue failure and would be difficult to apply in the real world. The continuous sinusoidal correction function was applied in the third case. Though the output power was less than the two preceding modifications, the feasibility of the third case made it the best option among the three modifications (Staelens, Saeed and Paraschivoiu, 2003).

In 2009, Paraschivoiu, Trifu and Saeed were computing the optimal variation of the blades' pitch angle of H-rotor in order to maximize the power coefficient at given conditions. The optimization procedure was conducted by a genetic algorithm optimizer, combined with DMSM codes. The optimized blade pitch enhanced the turbine performance at the design wind speed and in a relatively narrow wind speed domain around it. The pitch variation optimized in the low wind speed area could contribute an increase of 30% in the annual energy production of the turbine. However, when the wind speed changed, the optimized pitch was detrimental to the rotor performance. Thus, the optimizations of blade pitch at other wind speeds are required (Paraschivoiu, Trifu and Saeed, 2009).

Hwang *et al.* (2009) optimized the H-rotor by individual blade control with both experimental analysis and CFD simulations. The k-epsilon turbulence model was used in the 2D simulation. The power coefficient reached its maximum at a lower tip speed ratio

compared with experiment. By optimization of the individual blade control, the performance was improved by 25% (Hwang, Lee and Kim, 2009).

In 2010, Howell studied the performance of a small scale VAWT with both wind tunnel and CFD modeling (Howell, 2010). The experiments showed that the surface roughness on the turbine rotor blades had a great effect on the rotor performance. When the Reynolds number was below a critical value (Re=30,000), the rougher blade surface would enhance the rotor performance while above the value, the smoother blade surface would benefit the rotor performance. The investigation of two bladed and three bladed H-rotors showed that the turbine power coefficient was significantly higher for the rotors with higher solidity. The RNG k-epsilon turbulence model was used in both two dimensional and three dimensional simulations. The 3D modeling showed a reasonably good agreement with the experimental measurements while the 2D simulation showed an increased power performance compared with 3D simulations. The main reason was that both 3D simulations and experiments presented the existence of large tip vortices (Howell, 2010).

Some other optimizations were tried to improve the performance of H-rotors. A two dimensional analysis was carried out to evaluate the performance of a twisted three blade H-rotor. The standard k-epsilon turbulence model with moving mesh technique was applied to the simulation. The computational data presented a good match with experimental results. The optimal twist angle at the blade's trailing edge was determined by CFD model. Unlike the symmetric airfoil, the twist blade possessed positive lift at azimuth angle $\theta = 0$. For the twist bladed rotor, the self-starting capability was expected when azimuth angle $\theta \geq 90$ (Gupta, 2010).

In 2010, El-Samanoudy reported the effect of some design parameters on the performance of H- rotors by both wind tunnel experiments and CFD modeling. (El-Samanoudy, 2010) The pitch angle of their wind turbine varied from -10 degrees to 60 degrees. The performance of wind turbine increased as the pitch angle increased. After arriving at the peak performance, the power coefficient started to decrease. The effect of blade number was also investigated. The wind turbine performance increased significantly when the blade number increased from two to three. However, little increase was obtained when the blade number becomes four. The decrease of turbine radius resulted in a decrease of turbine performance as the interaction of blades became obvious. The symmetrical airfoil NACA 0024 gave a higher performance among the airfoils. The NACA 4420 and NACA 4520 showed little variation on power performance while NACA 0024 was much higher than both of them. The experiments also showed that increasing the chord length has a significant effect on the performance. In 2004, Bussel reported a skewed bladed VAWT prototype with an esthetic appearance and good performance (Bussel, 2004). In 2009, Takao reported that an H-rotor can be improved by adding a directed guide vane row. And the power coefficient was dependent on the distance between the guide vanes while independent of the number of guide vanes (Takao, 2009).

D. Research objectives

In this thesis, computational fluid dynamics is used to evaluate the aerodynamic performance of H-rotors. Both direct numerical simulation (DNS) and RNG $k - \varepsilon$ turbulence model are used to simulate the two dimensional model of H-rotors. The power,

25

torque, normal and tangential force coefficients are calculated and compared with experimental data to evaluate the prediction accuracy of CFD technique on such kind of problems. The prediction capability of the two different models is compared. The effect of blade interactions is investigated by comparing the force data from the blade of one bladed H-rotor and the blade of three bladed H-rotor. In order to obtain best power performance of the H-rotor, power coefficients are calculated at various tip speed ratios. The performance of blades with NACA0015 and NACA0022 airfoil sections are compared. The performance of H-rotors with a thicker airfoil section is expected to achieve better power performance.

II NUMERICAL METHODS

A physical flow field may be represented in terms of a mathematical model. The models must observe the fundamental properties of a flow field including conservation of mass, momentum and energy. Computational fluid dynamics uses various discretization schemes to approximate the governing equations of the flow field. The flow field is divided into certain number of cells which are called grids. Then the equations are solved at discrete grid points at each time step. By solving the governing equations simultaneously, the solution of the flow field can be obtained. The solution can be postprocessed to obtain the values of interest (e.g. lift, drag, torque, pressure loss, etc.).

A. DNS model

In this thesis, both Overture and Ansys Fluent CFD packages are used to solve the flow field equations. The Overture software uses direct numerical simulation (DNS) to solve the Navier-Stokes equations without any turbulence model with the finite difference schemes. In the fluid flow analysis, the compressibility of the flow will be considered when Mach number is larger than 0.3. The Mach number of flow around the H-rotor is much smaller than 0.3, so the flow will be considered as incompressible in the analysis. Therefore, the density of the flow will be constant. The time dependent incompressible Navier-Stokes equations can be written in differential form as:

27

$$\nabla \cdot \vec{u} = 0 \tag{2.1}$$

$$\frac{\partial \vec{u}}{\partial t} + \vec{u} \cdot \nabla \vec{u} = \frac{-\nabla p}{\rho} + \nu \nabla^2 \vec{u} \tag{2.2}$$

where ρ is the density, t is the time, $\vec{u}$ is the flow field velocity vector, p is the pressure, ν is the kinematic viscosity. The first equation corresponds to the continuity equation. The second equation is momentum equation which is obtained by applying Newton's Second law to a fluid passing through an infinitesimal control volume.

The finite difference scheme is applied to solve the time dependent incompressible Navier-Stokes equations. The method was developed by Henshaw (Henshaw, 1994). The formulation of the incompressible Navier-Stokes equations is solved on the structured overlapping grids.

In order to solve the equations, the initial conditions and boundary conditions shown below are needed.

$$\vec{u}(\vec{x}, 0) = \vec{u}_0(\vec{x}) \qquad \text{for } x \in D, t_0 = 0 \tag{2.3}$$

$$B(\vec{u}, p) = \vec{g} \qquad \text{for } x \in \partial D, t > 0 \tag{2.4}$$

The vector $\vec{x}$ represents the Cartesian coordinates in the computational domain D. The domain D is in R^N where N is the number of dimensions (either 2 or 3). ∂D is the boundary of the domain D. $\vec{u}$ is the velocity vector in Cartesian coordinates, p is the pressure and t is the time. $\vec{u}_0(\vec{x})$ represents initial condition in domain D. The boundary conditions are expressed as $B(\vec{u}, p) = \vec{g}$. A problem combining the continuity equation and conservation of momentum equation with initial and boundary conditions in the computation domain is called an initial boundary-value problem (IBVP) for the

28

incompressible Navier-Stokes equations. The system equations are also called the velocity-divergence formulation.

By taking the divergence of the momentum equation and using continuity equation, the pressure equation can be derived.

$$\frac{\nabla^2 p}{\rho} + \nabla u \cdot \vec{u}_x + \nabla v \cdot \vec{u}_y + \nabla w \cdot \vec{u}_z = 0 \qquad (2.5)$$

The elliptic pressure equation requires an extra boundary condition to make the problem well-posed. The boundary conditions and initial conditions are illustrated.

$$B(\vec{u}, p) = \vec{g} \qquad\qquad \text{for } x \in \partial D, t > 0 \qquad (2.6)$$

$$\nabla \cdot \vec{u} = 0 \qquad\qquad \text{for } x \in \partial D, t > 0 \qquad (2.7)$$

$$\vec{u}(\vec{x}, 0) = \vec{u}_0(\vec{x}) \qquad\qquad \text{for } x \in D, t_0 = 0 \qquad (2.8)$$

Combining the conservation of momentum equation and pressure equation, an alternative form of system equations is formulated, called the velocity-pressure formulation (Henshaw, 1994).

Also, the divergence damping term is added in the pressure equation (Henshaw, 2003).

$$\frac{\nabla^2 p}{\rho} + \nabla u \cdot \vec{u}_x + \nabla v \cdot \vec{u}_y + \nabla w \cdot \vec{u}_z - \alpha(\vec{x})\nabla \cdot \vec{u} = 0 \quad \text{for } x \in D, t > 0 \qquad (2.9)$$

where α is a coefficient to determine how much damping term will be added ($\alpha > 0$). The divergence damping term has no effect in the continuous case. But this term will be important to keep the dilatation small in the discrete case (Henshaw, 2003).

The system equations are discretized in space using second order central difference scheme. The result can be expressed as a system of ordinary differential equations.

$$\frac{d}{dt}\vec{u} = F(\vec{u}, t) \tag{2.10}$$

The pressure is considered to be a function of the velocity, $p = p(\vec{u})$. The equations are solved using an explicit time-stepping scheme (implicit scheme can also be used). The flow field can be obtained from pressure field and velocity field in previous time steps.

$$\vec{u}(t) = \vec{u}(*) + \alpha \Delta t F(\vec{u}(t - \Delta t), t - \Delta t) \tag{2.11}$$

where $\vec{u}(*)$ is the solution from previous time steps, and α is the same as equation (2.9). When giving $\vec{u}(t - \Delta t)$ and $\vec{p}(t - \Delta t)$ at all nodes and $F(\vec{u}(t - \Delta t), t - \Delta t)$ at interior nodes, the flow field could be solved at all interior nodes by making a time step. Then the value of $\vec{u}(t - \Delta t)$ at boundary and fictitious points are solved by using some of the boundary conditions. The pressure can be obtained by known velocity fields. Finally, $F(\vec{u}(t), t)$ is calculated at interior nodes for preparing the next time step calculation.

B. <u>Overlapping moving grid</u>

The blade rotating motion leads to a moving boundary problem. Therefore, a moving grid approach is required to dynamically update the computational grid to adapt to the blade motion. The overlapping moving grid is adopted (Henshaw, 2006) which uses overlapping grids to represent the flow geometry, including moving boundaries or

embedded boundaries. Boundary-conforming structured grids are used to achieve high-quality representations of boundaries. At the same time, Cartesian grids are employed as the background grids so that the efficiencies inherent with such grids can be exploited. The two kinds of grids are overlapped. The interpolation points located in the overlap region between different grids and are used to couple the solutions. At each time step, the boundary-conforming grids move together with the moving body according to the specified rotation. Only the interpolation points between grids must be recalculated as opposed to the need to regenerate the whole mesh, which may be necessary with other methods.

C. RNG k-epsilon model

The turbulence convected and dissipated in the flow field is generated due to various factors. The transported quantities including momentum, energy in momentum transfer and various concentrations in mass transfer are mixed in the turbulence due to the fluctuating velocity field. The fluctuations contain various scales and frequencies. Finer grids are required to capture the small scale fluctuations with high frequency. For turbulence simulation, the DNS model is both time consuming and computationally expensive.

The Reynolds Averaged Navier-Stokes (RANS) equations are used to solve the incompressible flow using a Boussinesq approach which relates the Reynolds stresses incurred by averaging the flow equations to the mean velocity gradients. In Reynolds averaging, the solution variables in instantaneous Navier-Stokes equations are divided

into the mean (ensemble average or time averaged) and fluctuating components. For the velocity components:

$$u_i = \bar{u}_i + u_i'$$ (2.12)

where $\bar{u}_i$ is the mean velocity components and u_i' is the fluctuating velocity components $(i = 1, 2, 3)$.

Likewise, for pressure and other scalar quantities:

$$\phi = \bar{\phi} + \phi'$$ (2.13)

where ϕ represents a scalar such as pressure, energy, or species concentration.

Substituting expressions of this form, the Reynolds averaged Navier-Stokes equations (RANS) can be obtained.

$$\frac{\partial \bar{u}_i}{\partial x_i} = 0$$ (2.14)

$$\rho \left(\frac{\partial \bar{u}_i}{\partial t} + \bar{u}_j \frac{\partial \bar{u}_i}{\partial x_j} \right) = -\frac{\partial \bar{p}}{\partial x_i} + \mu \frac{\partial^2 \bar{u}_i}{\partial x_j \partial x_j} - \frac{\partial}{\partial x_j} \left(\overline{\rho u_i' u_j'} \right)$$ (2.15)

These equations have the same general form as the instantaneous Navier-Stokes equations, with $\bar{u}_j$ representing the j component of mean velocity. x_j is the j coordinate. The Reynolds stresses, $\overline{\rho u_i' u_j'}$, must be modeled to close Equation (2.15).

The turbulence models chosen to close the RANS equations describing flow about the wind turbine blade section are the two equation $k - \varepsilon$ model. A transport equation which is defined in terms of turbulence kinetic energy is derived from the Navier-Stokes equation (Hinze, 1975). The turbulence kinetic energy (k) is the mean kinetic energy per unit mass associated with eddies in the turbulence flow. It can be calculated using

$$k = \frac{1}{2} \Sigma_i \overline{(u_i')^2}$$ (2.16)

where u_i' represents the fluctuating velocity in different directions.

32

The turbulence dissipation rate (ε) can be expressed by mean multiples of fluctuating velocity gradients.

$$\varepsilon = \frac{\partial k}{\partial t} = \nu \overline{(\frac{\partial u_i{'}}{\partial x_l})(\frac{\partial u_j{'}}{\partial x_l})} \tag{2.17}$$

where k is turbulence kinetic energy, t is time. $\frac{\partial u_i{'}}{\partial x_j}$ and $\frac{\partial u_j{'}}{\partial x_i}$ represent the fluctuating velocity gradient.

The transport equations derived from turbulence kinetic energy k and turbulence dissipation rate ε in RNG $k - \varepsilon$ are shown below (Yakhot, 1992).

$$\frac{\partial(\rho k)}{\partial t} + \frac{\partial}{\partial x_i}(\rho k u_i) = \frac{\partial}{\partial x_j}\left(\alpha_k \mu_{eff} \frac{\partial k}{\partial x_j}\right) + G_k + G_b - \rho\varepsilon \tag{2.18}$$

$$\frac{\partial}{\partial t}(\rho\varepsilon) + \frac{\partial}{\partial x_i}(\rho\varepsilon u_i) = \frac{\partial}{\partial x_j}\left(\alpha_\varepsilon \mu_{eff} \frac{\partial \varepsilon}{\partial x_j}\right) + C_{1\varepsilon}\frac{\varepsilon}{k}(G_k + G_b) - C_{2\varepsilon}^*\rho\frac{\varepsilon^2}{k} \tag{2.19}$$

where G_k represents the generation of turbulent kinetic energy due to the mean velocity gradients, G_b is the generation of turbulence kinetic energy due to buoyancy. The quantities α_k and α_ε are inverse effective Prandtl numbers for k and ε.

The momentum transfer caused by turbulent eddies could be modeled with an eddy viscosity. The eddy viscosity is a function of the flow. If the turbulence is more intense, it becomes larger. The eddy viscosity can also be expressed in terms of turbulence intensity (I) and turbulence length scale (l). These scales are derived from turbulence kinetic energy (k) and dissipation rate (ε). Both turbulence intensity and turbulence length scale can be obtained by empirical equations.

Turbulence intensity:

$$I = (\frac{2}{3}k)^{\frac{1}{2}}/\overline{U} \tag{2.20}$$

where $\overline{U}$ is the mean flow velocity.

33

Turbulence length scale:

$$l = \frac{k^{\frac{3}{2}}}{\varepsilon}$$

(2.21)

Eddy viscosity(μ_t) can be expressed as

$$\mu_t = \rho C_\mu \frac{k^2}{\varepsilon} = 1.225 \rho C_\mu \bar{U} l l$$

(2.22)

$$\mu_{eff} = \mu + \mu_t$$

(2.23)

where C_μ is a dimensionless constant, v is the velocity scale and l is the length scale of the turbulence, μ_t is the eddy viscosity.

$C_{2\varepsilon}^*$ is given by

$$C_{2\varepsilon}^* = C_{2\varepsilon} + \frac{C_\mu \rho \eta^3 (1 - \frac{\eta}{\eta_0})}{1 + \beta \eta^3}$$

(2.24)

The six adjustable constants (except β) are derived explicitly in the RNG procedure.

$C_\mu = 0.0845$ $\qquad$ $C_{1\varepsilon} = 1.42$ $\qquad$ $C_{2\varepsilon} = 1.68$

$\eta_0 = 4.38$ $\qquad$ $\alpha_k = \alpha_\varepsilon = 1.39$ $\qquad$ $\beta = 0.012$

The turbulence Renormalization Group k − ε model (RNG k − ε) is adopted in Ansys Fluent to study the two-dimensional simulation. The model was proposed by Yakhot in 1992 (Yakhot et al., 1992). In this model, the rigorous statistical technique is applied to instantaneous Navior-Stokes equations to capture the effect of smaller scale motions (Pezzinga, 1994). Compared with the standard k − ε model, the refinements are made as follows (Fluent 2002).

- The RNG model has an additional term in its ε equation for interaction between turbulence dissipation and mean shear that significantly improves the accuracy for rapidly strained flows.

- The effect of swirl on turbulence is included in the RNG model, enhancing accuracy for swirling flows.

- While the standard k- ε model is a high-Reynolds-number model, the RNG theory provides an analytically-derived differential formula for effective viscosity that accounts for low-Reynolds-number effects. Effective use of this feature does, however, depend on an appropriate treatment of the near-wall region.

The eddy viscosity is a kind of numerical model to evaluate the turbulence diffusion. The eddy viscosity is determined from a specified single turbulence length scale in the standard $k - \varepsilon$ model. The transport equations in RNG $k - \varepsilon$ model determine different scale motions when the production term changes. Therefore, better results can be obtained using the RNG $k - \varepsilon$ model for more complex behavior, such as separating flows, jet impingement, secondary flows and swirling flows (Fluent, 2006).

D. Sliding mesh

Sliding mesh technique is applied to describe the rotating motion of the wind turbine blades. The sliding mesh formulation allows adjacent grids to slide relative to another stationary frame, so the grid faces do not need to be aligned on the grid interface. The situation requires a means of computing the flux come across the two non-conformal interface zones of each interface. The intersection between the interface zones is determined at each new time step to compute the interface flux.

35

The rotating motion of the moving CFD domain is shown in Figure II-1. The motion of any point in the rotating domain is expressed by a time rate of change of the position vector ($\dot{\vec{r}}$), which is also known as the grid speed. For rigid body rotation at constant speed

$$\dot{\vec{r}} = \vec{\omega} \times \vec{r} = \vec{V} \tag{2.25}$$
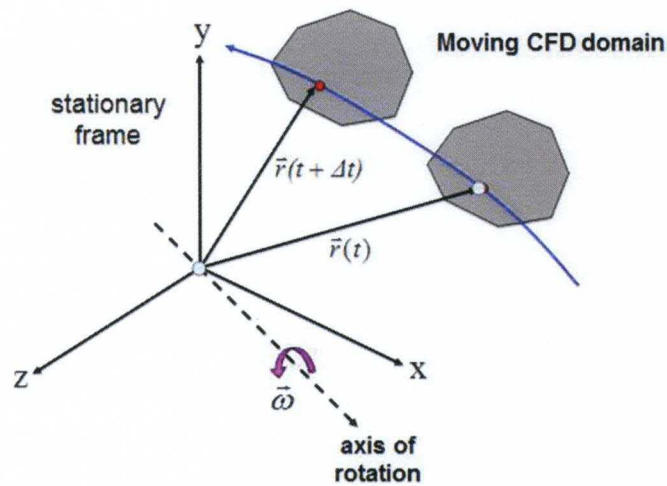
Figure II-1 Moving mesh illustration

In the rotating region, a set of modified balance equations are solved.

$$\nabla \cdot (\vec{u} - \vec{V}) = 0 \tag{2.26}$$

$$\frac{\partial \vec{u}}{\partial t} + \vec{u} \cdot \nabla(\vec{u} - \vec{V}) = \frac{-\nabla p}{\rho} + \nu \nabla^2 \vec{u} \tag{2.27}$$

Here $\vec{u}$ is the liquid velocity in the stationary frame and $\vec{V}$ is the velocity component arising from mesh motion. p is the pressure and ν is the kinematic viscosity. Equation (2.26) is the modified continuity equation and the equation (2.27) is the modified equation of momentum conservation. At the sliding interface a conservative

36

interpolation is used for both mass and momentum, using a set of fictitious control volumes. Therefore, the flow field solution can be obtained.

III   NUMERICAL SIMULATION WITH DNS MODEL

In this section, the numerical simulations using Overture are presented and analyzed. Ogen, the grid generation tool inside of Overture generate the H-rotor grids and assemble overlapping grids. First, the geometry and grid components are generated by the user. Then the grid generation tool detects all grid points to be removed. Third, all grid points used for interpolation are located on the edge of the removed points. More detail process is presented in Henshaw's (2005) paper. Finally, the consistency of the system is checked to see if it satisfies all the requirements. If not, all the failed points outputted as a graphic for troubleshooting. When the grid is successfully built, Cgins, the CFD solver will be utilized to solve the fluid field by DNS methods which has described in numerical methods.
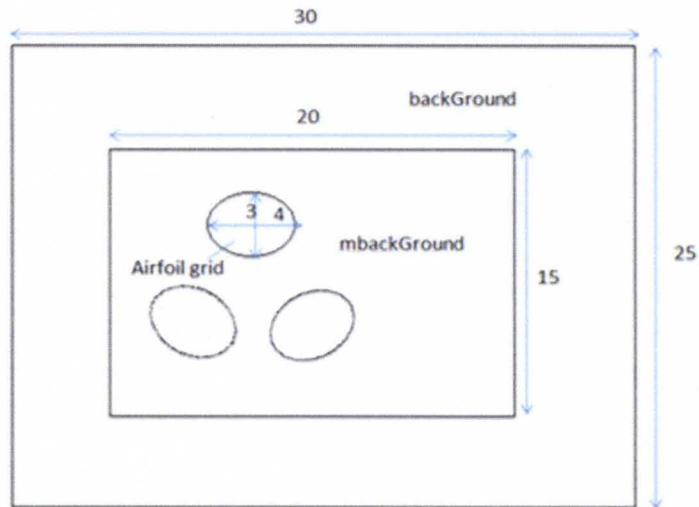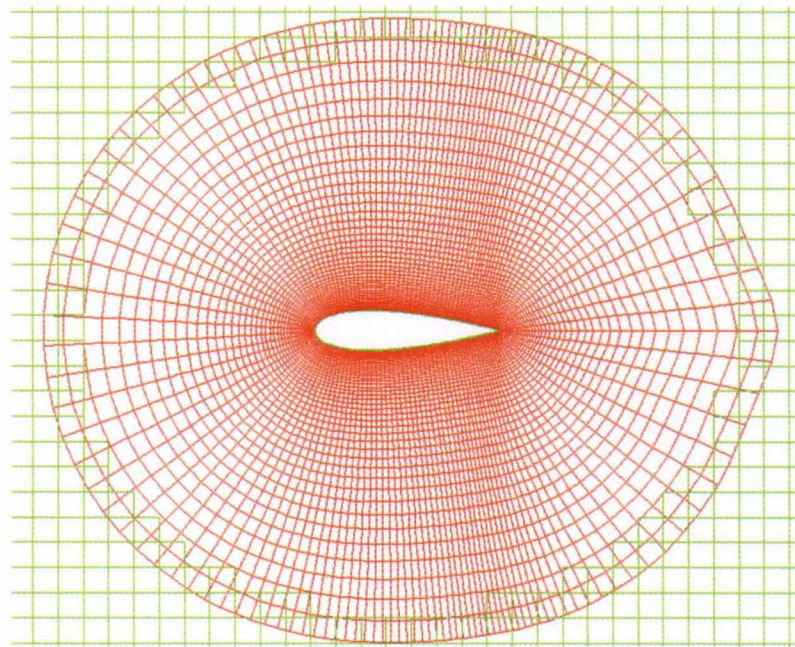

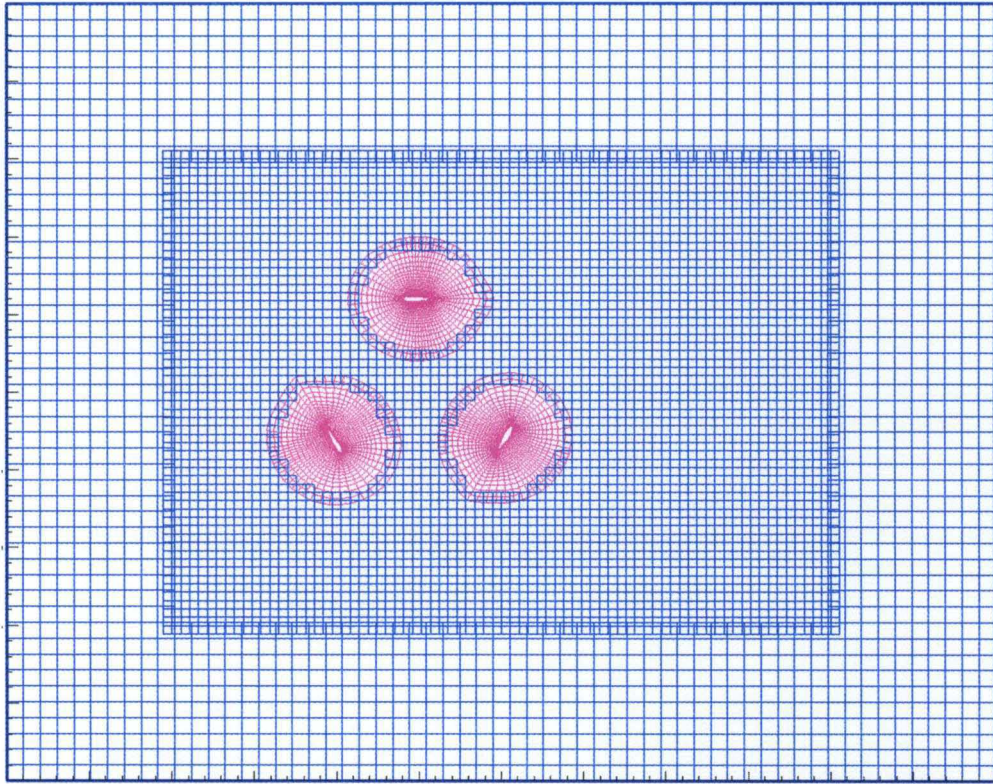**Figure III-1 Computational domain of the H-rotor**

A. Grid generation

The computational domain includes a background domain and a medium background domain and the rotating blade domain. Figure III-1 shows us the computational domain with size parameters of the 2D three bladed H-rotor. The domain is large enough to capture the aerodynamic performance of the airfoil blade. NACA0022 profile is used for blade section and the solidity of the rotor is 0.33.

The body fitting grids were generated around the airfoil. Figure III-2 shows us the body fitting grid surrounding the airfoil. The Cartesian grids were employed to generate the background grids and medium background grids. Then the airfoil grids were overlapped at the center of the medium background grids and then these overlapped grids again were overlapped at the center of the background grids. The complete grid system is shown in Figure III-3.

**Figure III-2 Body fitting grids around airfoil**

Figure III-3 The overlapping grids of the whole computational domain

Before the simulation, the boundary conditions should be set. The left side of the domain was set as velocity-inlet and the right side was set as pressure-outlet. Both top and bottom boundaries were set as noslip walls to simulate the condition of wind tunnel. The boundary of airfoil blade was also set as noslip wall. The Reynolds number was based on the chord length of the airfoil, the kinematic viscosity and inlet velocity. Due to the limitation of DNS modeling, the Reynolds number in the simulation was set as 5000 while the Reynolds number is usually larger than 30000 in really world. The artificial diffusion was also added to adjust the solution.

B. Sensitivity analysis

The density of grids is one of the most important factors affecting the simulation results. Therefore, the sensitivity analysis should be done for each subdomain. When doing sensitivity analysis for one domain grids, other domain grids are fixed. The background grid resolution is expressed as $a \times b$, where a is the number of grid points in x direction and b is the number of grid points in y direction. For airfoil grids, a is the number of grid points in circumferential direction and b is radial direction nodes number. Figure III-4 shows the airfoil shape and the grid density direction definition.
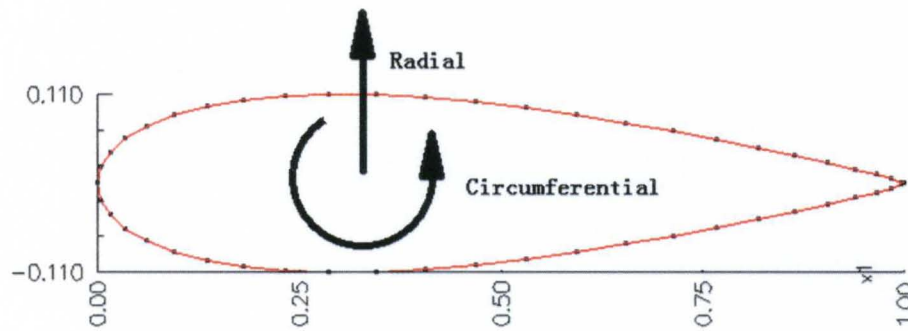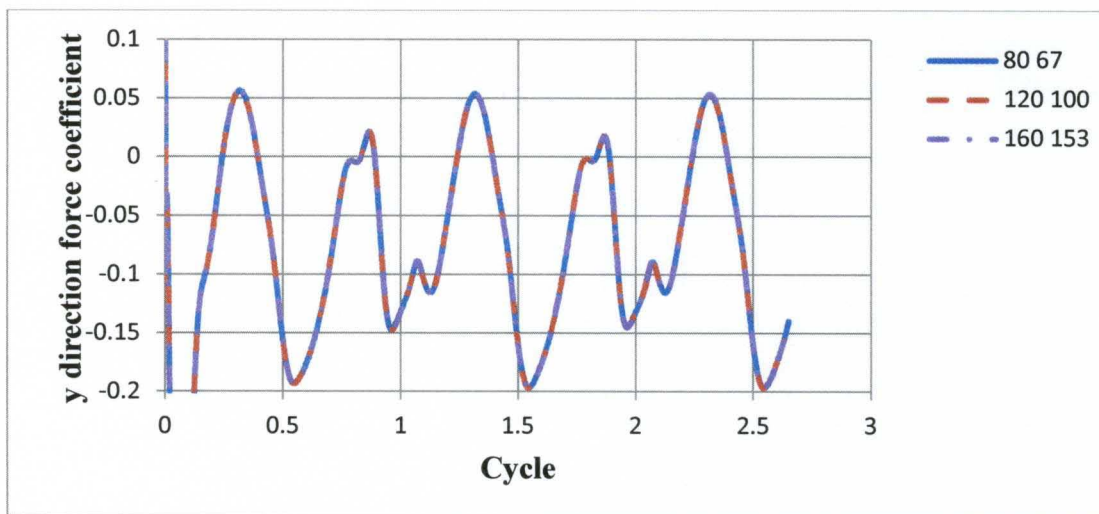

Figure III-4 Direction definition

The effect of different background grid resolutions was tested. The grid density used for background grid sensitivity analysis is shown in Table III-1. Three different background grid resolutions were tested, 80×67, 120×100 and 150×133. The computational results are shown in Figure III-5 and Figure III-6 where there is almost no variation of between these three grid resolutions. As the background is far away from the rotating blade, the density of the background grid doesn't give computational performance on the rotating blades. The 80×67 and 120×100 grids could be used

41

without altering the results significantly from the 150×133 grid. In this chapter, the 120×100 grid points are applied.

Table III-1 The number of grids for background grid sensitivity analysis

	backGround	mbackGround	airfoil grid
Grid 1	80×67	150×113	160×53
Grid 2	120×100	150×113	160×53
Grid 3	160×133	150×113	160×53

Figure III-5 The y direction force coefficient vs. cycle of various background grids
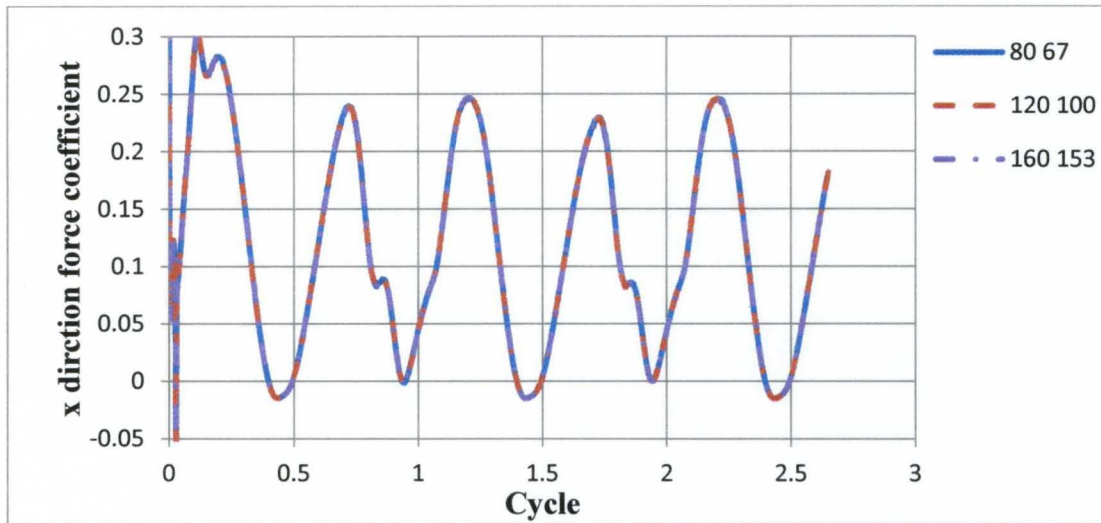
Figure III-6 The x direction force coefficient vs. cycle of various background grids

The effect of medium background grids was tested. The grid points applied on each direction for medium background grid sensitivity analysis is shown in Table III-2. The medium background grid resolutions were tested with 100×75, 150×113 and 200×150. The computational results are shown in Figure III-6 and Figure III-7. Though the grid density showed minor effect on the results, the impact of medium background grid was more obvious as it is closer to the rotating blades than background grid. But the mbackground grids were still away from the rotating motion compared with the airfoil grid. Considering both computing and economical efficiencies, the 150×113 grids are applied for the medium background grid.
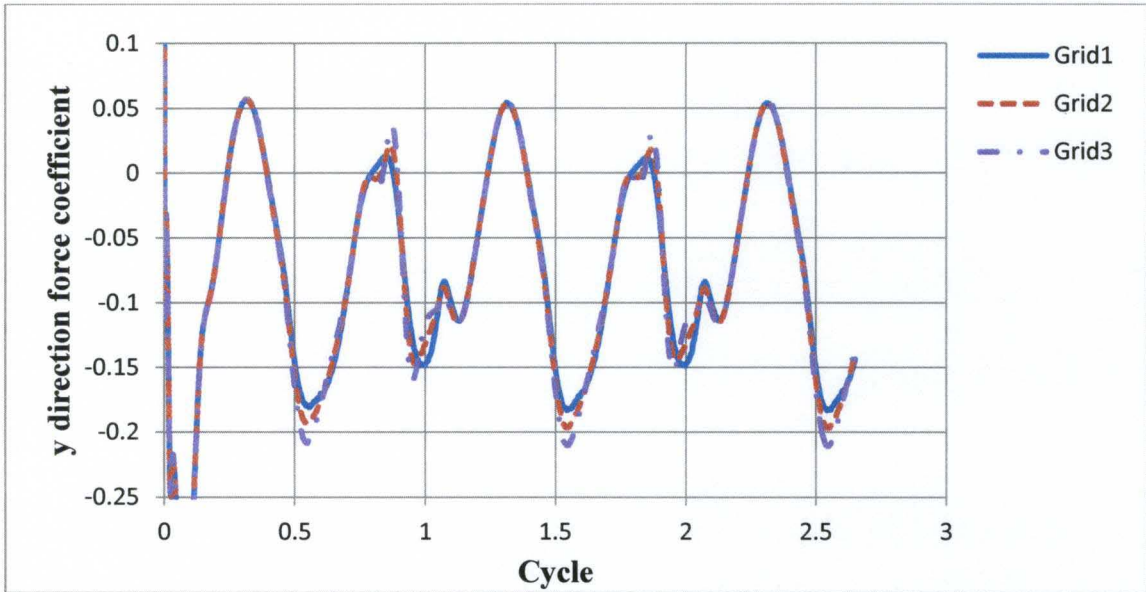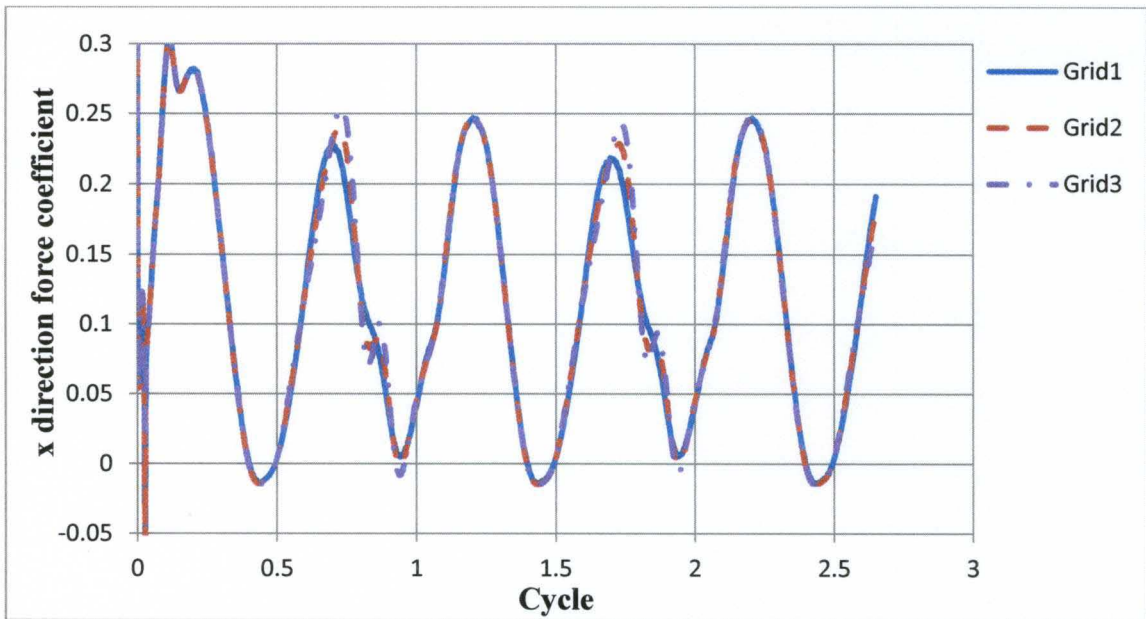
Table III-2 The number of grids for medium background grid sensitivity analysis

	backGround	mbackGround	airfoil grid
Grid 1	120×100	100×75	160×53
Grid 2	120×100	150×113	160×53
Grid 3	120×100	200×150	160×53

43

Figure III-7 The y direction force coefficient of various mbackground grids
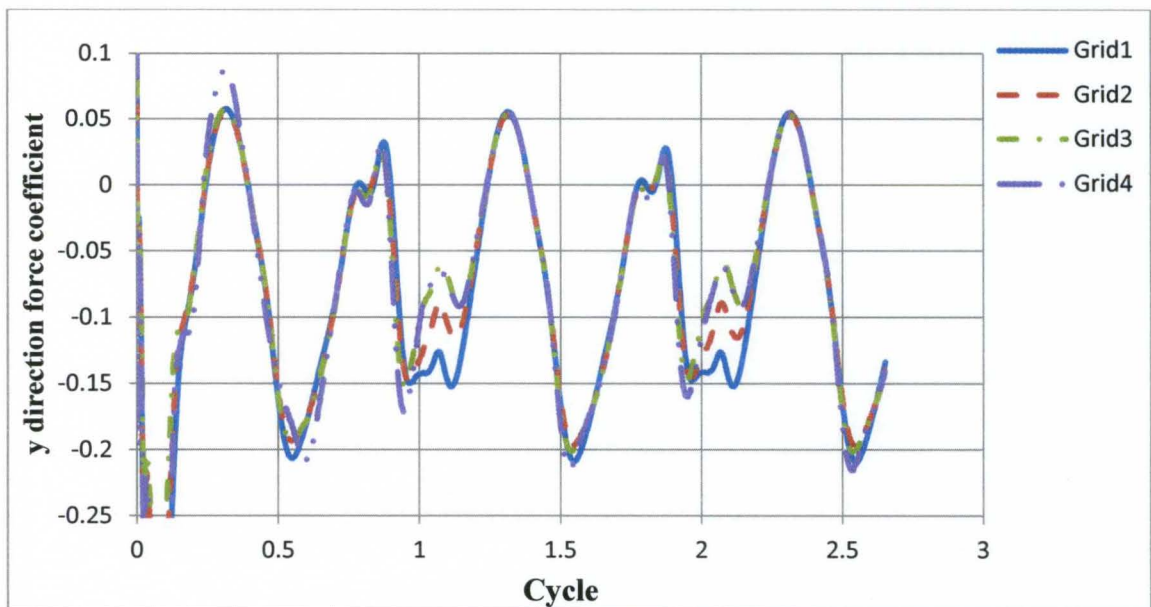

Figure III-8 The x direction force coefficient of various mbackground grids

The airfoil grid is the closest to airfoil blades. A little change of the air grid might cause a significant impact to the airfoil performance. The testing airfoil grids are carried

44

out using $138 \times 46, 160 \times 53$, 195×60 and 250×83. Table III-3 lists the grid density of doing airfoil grid sensitivity analysis. The results from 195×60 and 250×83 are very similar. However, their computational time is quite different. For the grid of 250×83, it almost took two weeks to finish the simulation while the 195×60 just spent one week. Therefore, 195×60 is applied as airfoil grid density.

Table III-3 The number of grids for airfoil grid sensitivity analysis

|	backGround	mbackGround	airfoil grid
Grid 1	120×100	150×113	138×46
Grid 2	120×100	150×113	160×53
Grid 3	120×100	150×113	195×60
Grid 4	120×100	150×113	250×83

Figure III-9 The y direction force coefficient vs. cycle of various airfoil grids

45
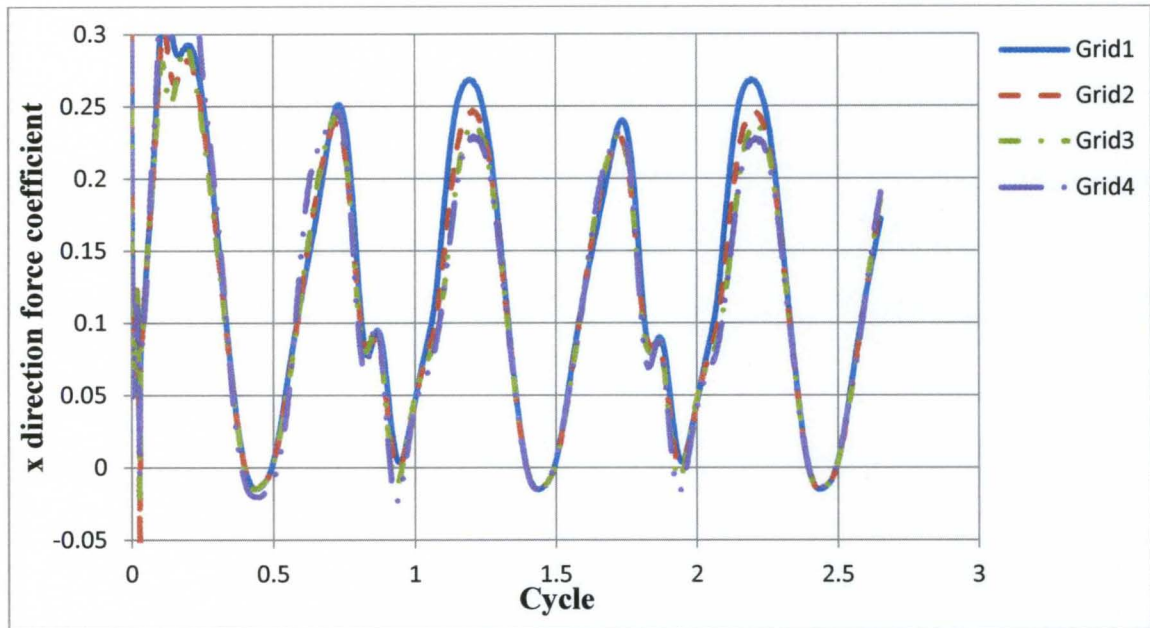
Figure III-10 The x direction force coefficient vs. cycle of various airfoil grids

From Figure III-9 and Figure III-10, it was found that the variations always occurred at the beginning of one cycle where the azimuth angle $\theta < 45^o$. The streamlines at these positions were plotted. Figure III-11 shows the streamline plot at $\theta = 11°, 22°, 33°$ and $45°$. The vortex shedding process during the rotation was observed in these figures. The vortex shedding could be a reason that the model didn't capture the aerodynamic performance of blade airfoil precisely at these positions. Besides, in this area the blade rotated to windward where the real Reynolds number calculated from relative velocity at these positions was much higher than 5000, so the flow was unsteadier. It is hard to capture the performance at such high Reynolds number by DNS model.
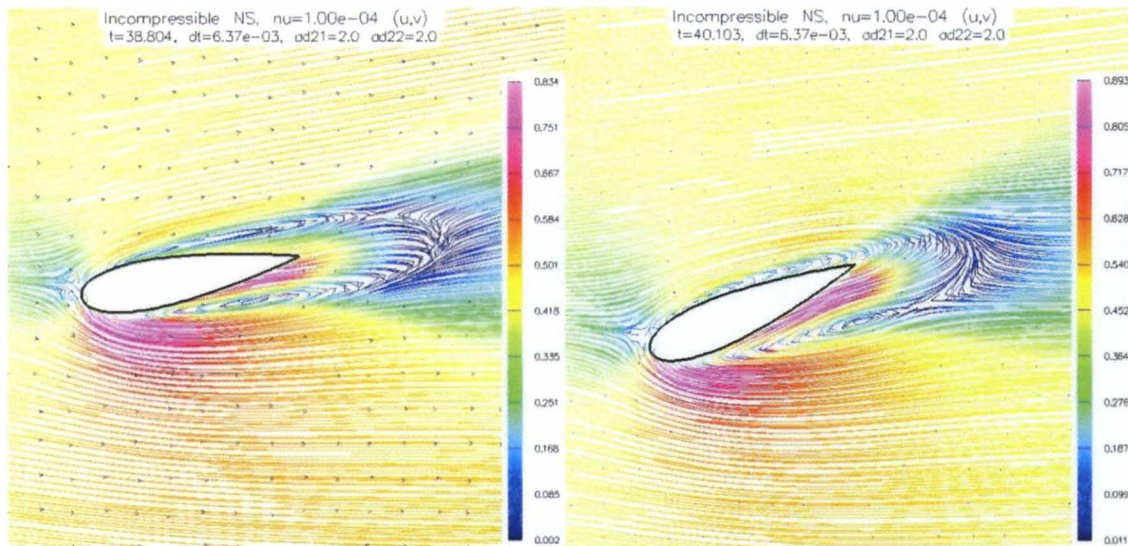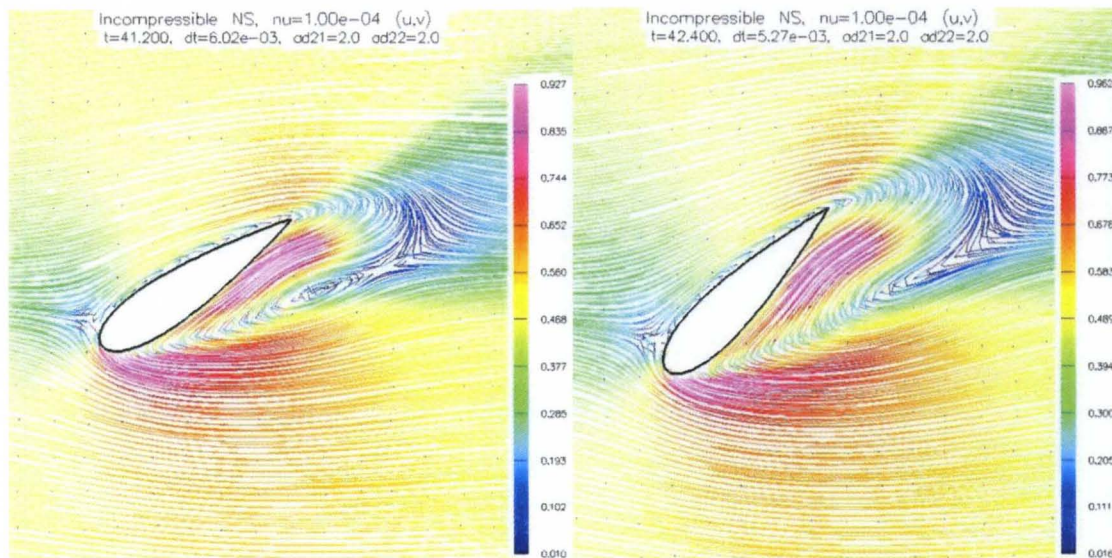
Figure III-11 (a)Streamline plot at θ = 11°; (b)Streamline plot at θ = 22°; (c)Streamline plot at θ = 33°; (d)Streamline plot at θ = 45°.

Though the result based on the airfoil grids is converged finally, the force data are still showing great difference with the experimental data. The variations shown above are just happen at TSR=1. When modeling high TSRs, the convergence at much higher Reynolds number brought more problems. In the DNS model, the maximum power TSR

could not be predicted by this model. The characteristic trend of the wind turbine rotating

performance could not be captured by the simulation at Re=5000. It might be that the grid

density is not enough to capture the performance. However, if denser grids are used, it

would take more time to finish one case which is not economical enough for the research.

Another reason might be that the aerodynamic performance of the H-rotor is sensitive to

the Reynolds number. Furthermore, when applying high Reynolds number, the

convergence would be a big problem. Therefore, the DNS isn't suitable to analyze the

aerodynamic performance of H-rotors.

IV NUMERICAL SIMULATION WITH RNG $k - \varepsilon$ MODEL

A. Simulation procedure

The mesh generation in this thesis was carried out using Gambit. This software can be used for the creation of structured and unstructured grids. The domain of wind turbine was divided into six subdomains. The six subdomains are shown in Figure IV-1. The moving mesh formulation would be applied to the rotating area to approximate the motion of airfoil blades.
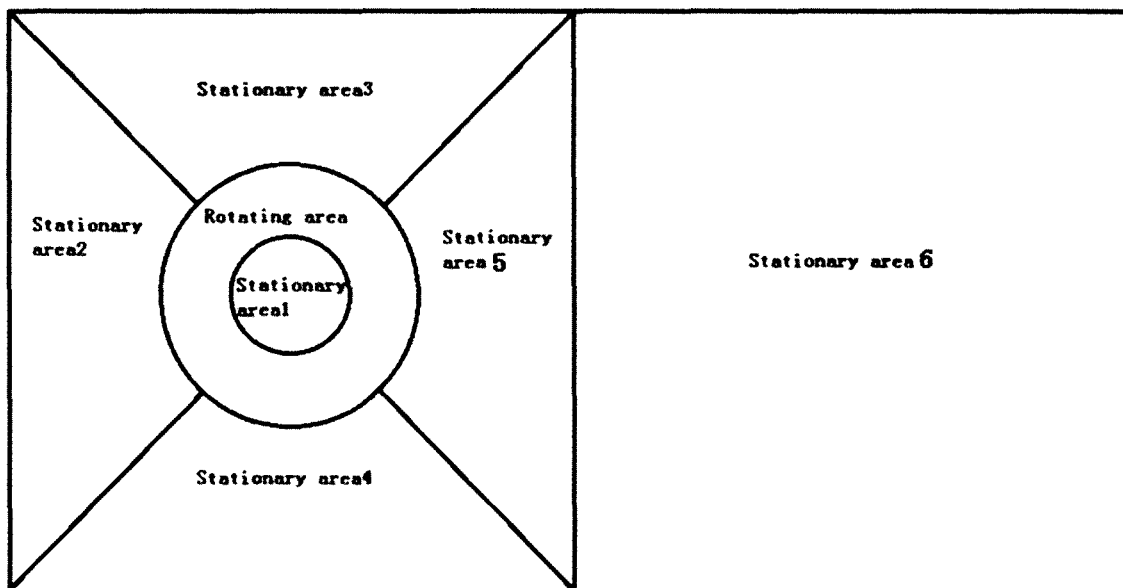
Figure IV-1 Seven subdomains in the modeling area

The mesh of the whole domain is shown in Figure IV-2. Both structured and unstructured grid technique were adopted to create the simulation grids. For structured

grids the domain is rectangular in shape where the interior grid points are distributed along the grid lines, so the grid point could be easily identified in reference to the grid line. The main advantage of structured grids is the high degree of user control which enables users to concentrate the grid points in the regions of complex flow, such as boundary layer. As a result of optimizing grids density, the computational efficiency can be improved significantly. The unstructured grids are the exact opposite of structured grids, where the connectivity between points must be explicitly defined for every set of points. In another word, the unstructured grids are typically defined as points and cells. The cells can be either tetrahedral or quadrilateral. The unstructured can be conveniently applied to irregular areas.
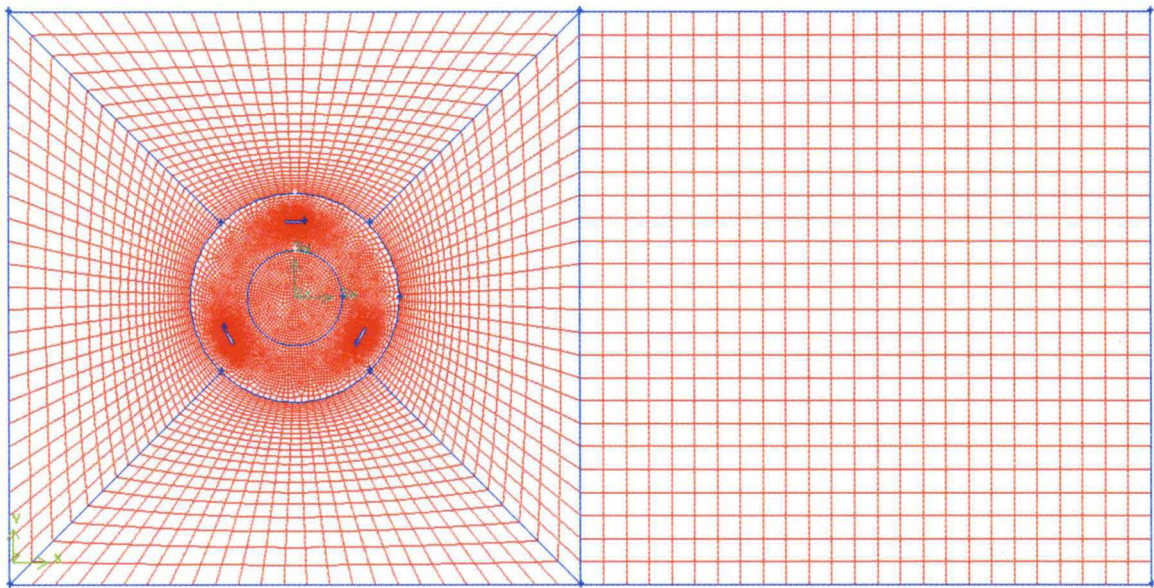

Figure IV-2 Fully unstructured fluid domain

In the fluid domain, the stationary area 2, 3, 4, 5 and 6 are rectangular or could be considered as rectangular in topology, so that the structured grid can be applied in these areas. Each boundary of the structured grid subdomains contained 50 grid points. The

unstructured mesh was adopted in moving area and stationary area 1 due to their irregularity. 200 grid points was set on the boundary of stationary area 1. Each boundaries of the rotating area had 200 grid points and also the airfoil boundary was defined with 200 grid points. Figure IV-3 shows the unstructured grids in the moving area and stationary area 1. The quadrilateral mesh was concentrated in the rotating subdomain around the rotor with 51201 computational cells and the stationary subdomains contain 15983 cells totally. A detail view of the grid surrounding the airfoil presents in Figure IV-4. The airfoil was placed at the center circle of the moving area.
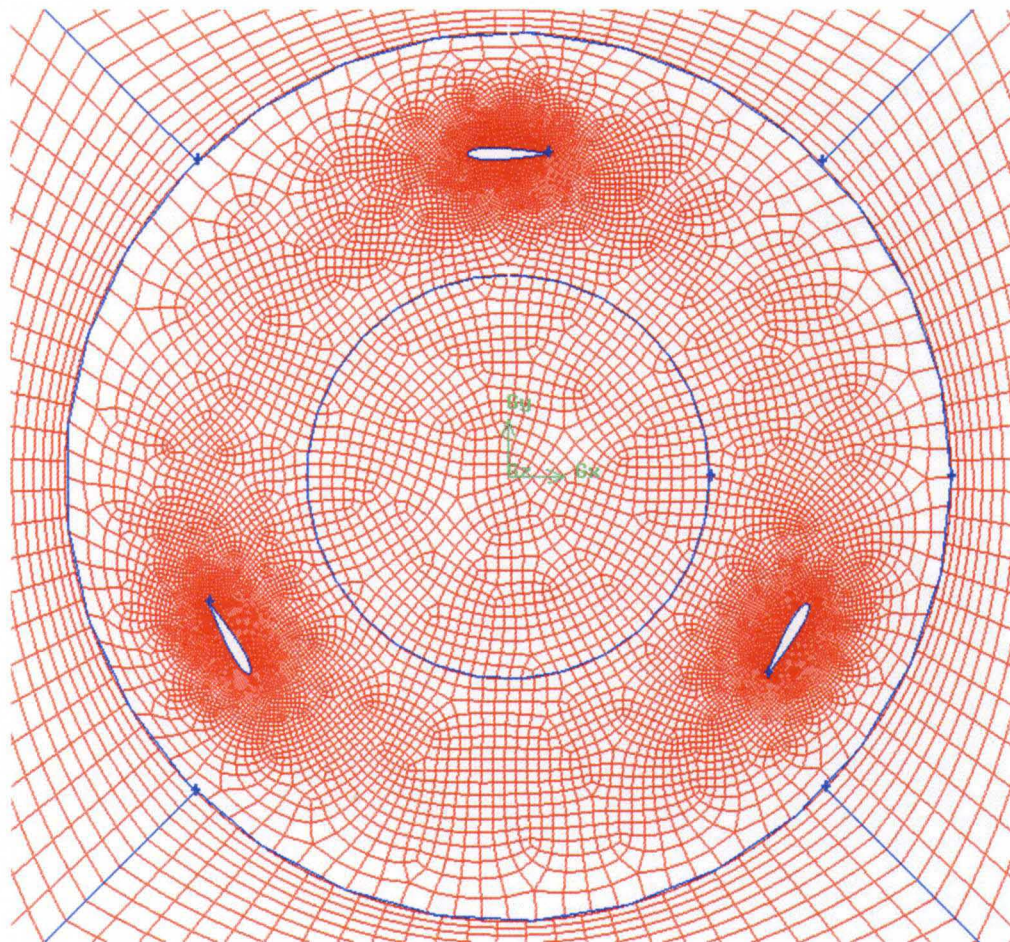
Figure IV-3 Unstructured quadrilateral mesh of stationary area 1 and rotating area
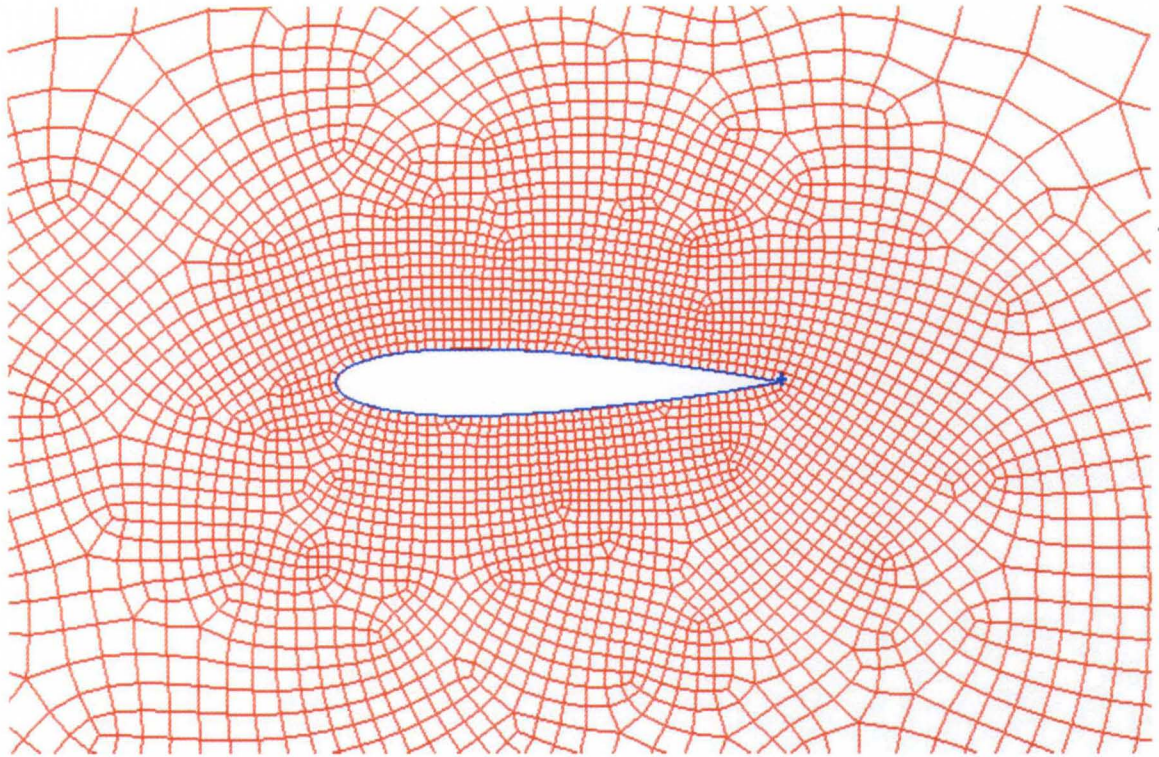
Figure IV-4 Detail view of fully unstructured airfoil mesh

The simulations were done with the commercial CFD package, Fluent. RNG $k - \varepsilon$ turbulence model was applied to the simulation. The solution methods are presented in Table IV-1. The entrance of the fluid domain was specified as a velocity inlet boundary. The absolute magnitude of the inlet velocity was set as 3.9m/s, the mean wind speed in Kentucky area. Based on the chord length, Reynolds number was 26800 and the solidity was 0.25. Pressure outlet was applied as the boundary condition of the right wall. And the top and bottom walls were set as no slip wall boundaries. The turbulence intensity was set as 4.4% and the turbulence length scale is 0.77.

Table IV-1 Solution method for 2D simulation of H-rotor

Solution Parameter	Solution Method
Pressure-Velocity Coupling Scheme	Semi-Implicit Method for Pressure-Linked Equations (SIMPLE)
Spatial Discretization Gradient	Least Squares Cell Based
Spatial Discretization Pressure	Standard
Spatial Discretization Momentum	Second Order Upwind
Spatial Discretization Turbulent Kinematic Energy	Second Order Upwind
Spatial Discretization Turbulent Dissipation Rate	Second Order Upwind
Transient Formulation	Second Order Implicit

The six stationary areas were identified as fluid zones with stationary mesh while the annulus containing airfoil blades was classified as fluid zone with moving mesh. The motion of the moving mesh was specified with a certain angular velocity determined by the TSR. The rotation direction was in positive z-direction. The interfaces between all the subdomains were defined as interior boundaries. The turbine blades were identified as no slip walls and they were set as stationary relative to the rotating grids.

B. Simulation results

In this section, the results from the CFD simulations are presented and analyzed. The instantaneous force coefficients on the airfoil blade are compared with previous published research to discuss deviation or agreement with the literature. The performance of three bladed and one bladed H-rotor is compared to study the interactions between the

blades. Then, the aerodynamic performances of wind turbines with different airfoil section blades are compared.

1. One bladed H-rotor

The same size grids were generated to model the Oler's experiment (1983) with one blade at the same flow conditions and geometric features to validate the CFD simulation. The experiments were carried out in water tunnel with both pressure and strain gage measurements. In the pressure measurement the pressure ports were placed at ten locations on airfoil surface with a uniform depth of about 30cm below the water surface. And the strain gages were located on a support mounted at the mid chord. In the water tunnel experiments the Reynolds number was 67,000 based on the tip speed and airfoil chord length. The solidity was 0.25. In their experiments, the rotating speed of the blade was kept constant while changing the flow velocity to achieve different TSRs. The case of TSR=2.5 was modeled. When the TSR=2.5, the Reynolds number was 26800 based on the flow velocity and chord length.
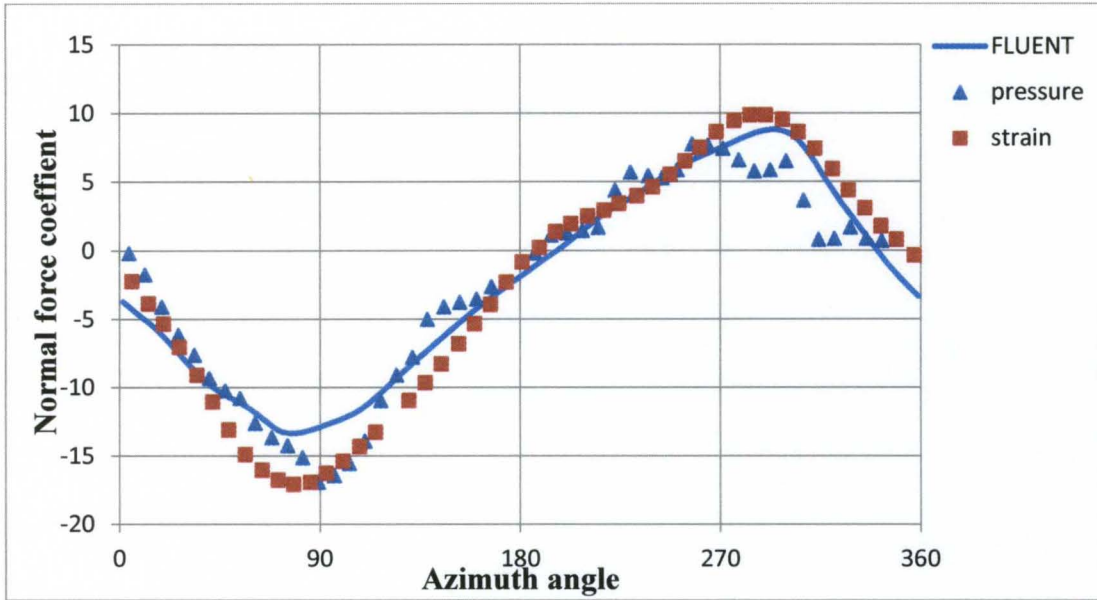
Figure IV-5 The normal force coefficient vs. azimuth angle
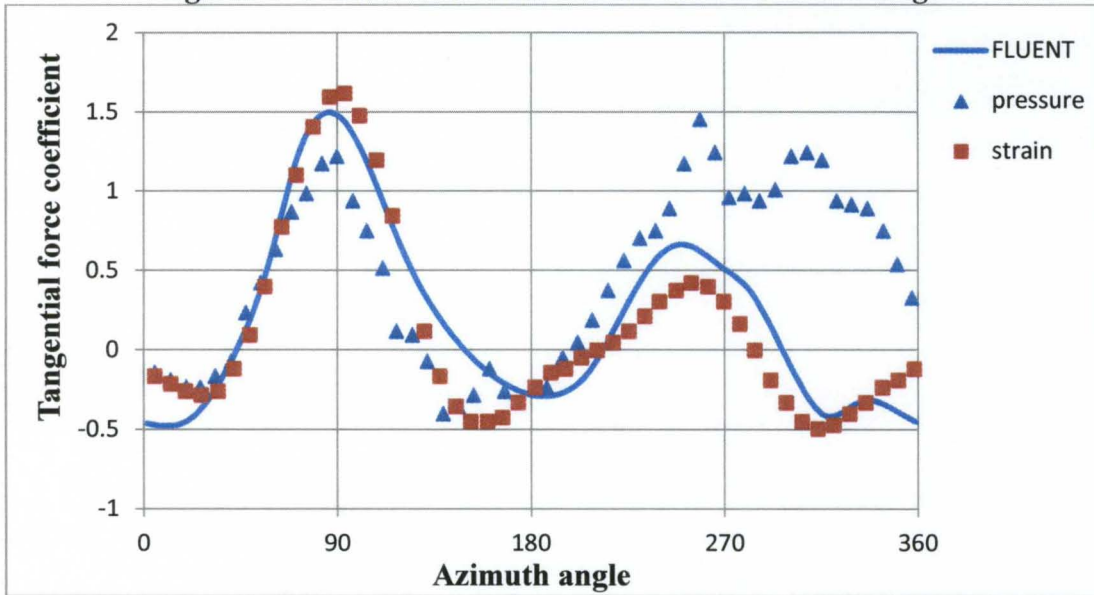
Figure IV-6 The tangential force coefficient vs. azimuth angle

Figure IV-5 and Figure IV-6 display the normal and tangential force coefficients plotted against azimuthal position in both experimental data and simulation results. In pressure measurement, force coefficients were obtained by integrating the pressure data

from ten pressure port while the strain gauge measurement calibrated force data for the whole blade. This caused the deviation between strain gage and pressure measurement showing in both Figure IV-5 and Figure IV-6.

It was found that the normal force coefficients were close to the experimental results in Figure IV-5. In Figure IV-6, the tangential force coefficients were analogous to the experiment data in the first quarter period. However, the discrepancies increased during the second quarter period. In this area, the leading edge separation happened which cannot be precisely captured by the turbulence model. Ferreira (2007) pointed out that the turbulence models suppressed the development of the leading edge separation. In the last two quarters, the simulation results still showed a little difference compared with the experimental data. The dynamic stall also happened in these areas. Another reason caused some little difference is that the aspect ratio used in Oler's experiment (Oler, 1983) was low and a 3D simulation might be requirable. Overall, the RNG $k - \varepsilon$ model was reliable to predict the aerodynamic performance of H-rotors. And the sliding mesh could capture the instantaneous interaction between the rotating turbine and the flow around it.

2. Three bladed H-rotor

Then the turbulence model was applied to simulate the 2D H-rotor with three blades. The blade number is also an important factor to power performance. Apparently more blades can bring more power generated if there is no interaction between blades. However, the flow from the upstream blade will have impact on the airfoil downstream obviously. As a result of the influence of blades interactions, the rotor could achieve the maximum power output with a certain blade number. Besides, as more blades added on

56

the rotor, more strength is required to support the rotor. These will bring problems to the strut and the supporting arms design. In this thesis, three blades were chosen in the simulation.
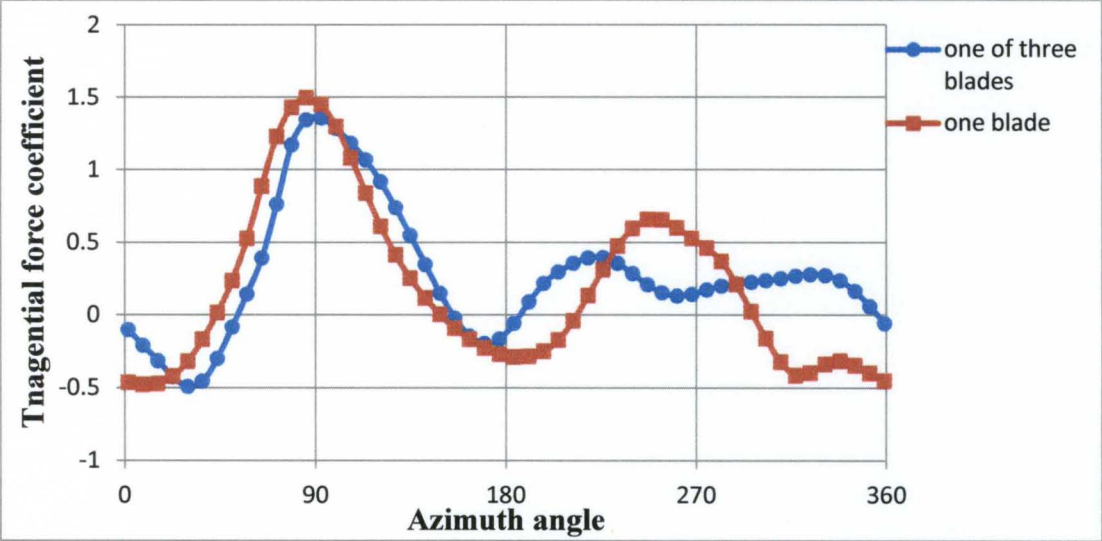

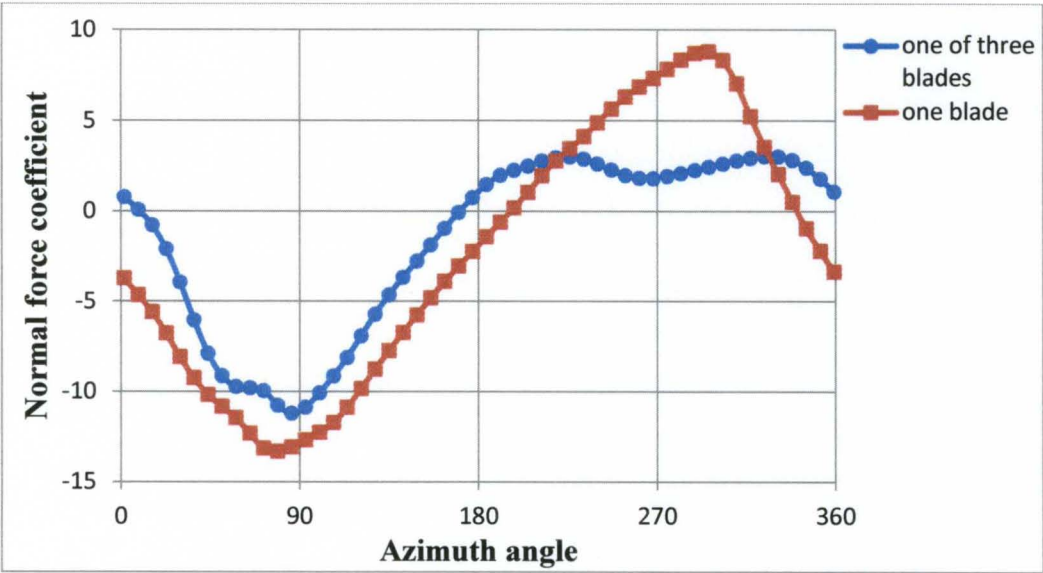**Figure IV-7 Tangential coefficient of H-rotor with one blade and three blades**

Figure IV-8 Normal coefficient of H-rotor with one blade and three blades

Figure IV-7 and Figure IV-8 show the tangential and normal force coefficient plot vs. azimuth angle of three bladed and one bladed H-rotors. There was not any significant variation between the two curves in the upstream. When it came to the downstream, the vortex shedding from upstream had an obvious impact on the blade in the downstream.
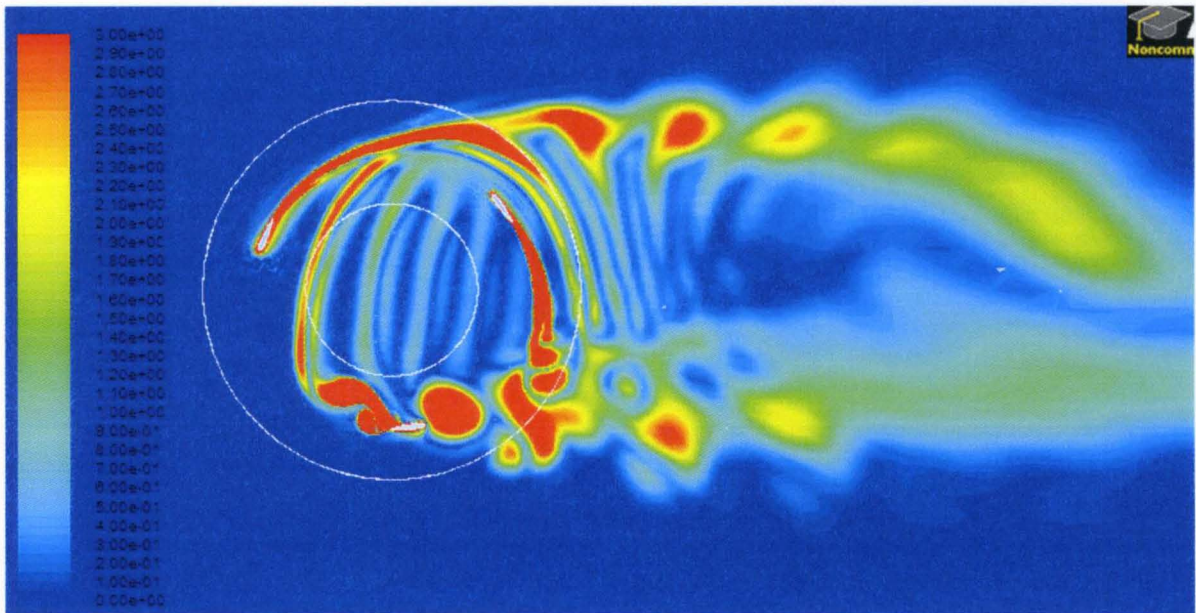
Figure IV-9 Contours of vorticity in the flow field around the H-rotor

Figure IV-9 shows the contour plot of vorticity. The vortices were in the large area of downstream while there weren't much significant vortices in the upstream. Therefore, most variations between the turbines happened in the downstream. Though the blade of one bladed H-rotor might be affected by the vortices generated by itself in previous period, the time interval is three times of that of three bladed H-rotors. The vortices generated in this cycle won't contain much energy in next cycle.
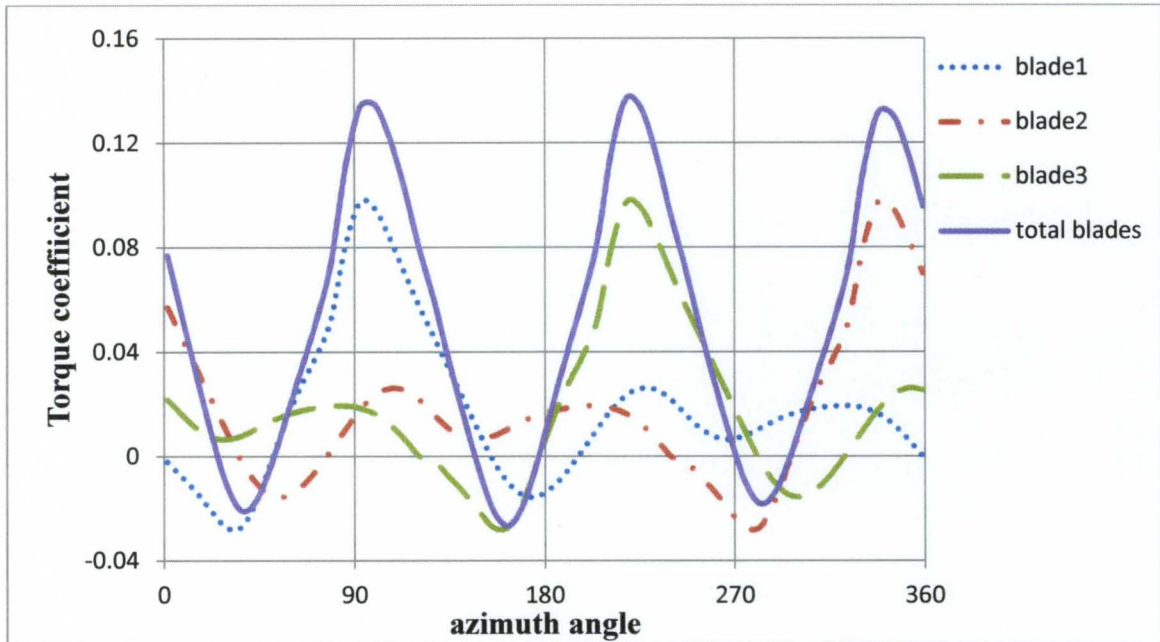
Figure IV-10 Torque coefficient of each blade and total blades

Each blade can generate certain amount of torque by the tangential force. At azimuth angle $\theta = 0$ degree, negative torque was generated. At about $\theta = 30^o$ degrees, the torque reached its minimum value. At this position, the angle of attack was so small that the lift could only make small contribution to generate torque. After then, torque began to increase due to the lift direction was preferable to make more contribution to the positive torque and the lift was also increase with the angle of attack. As a result of the increasing angle of attack, the dynamic stall happened. The torque achieves its maximum value at $\theta = 90^o$ after stall. After the peak, the tangential force decreased as the direction of the blade was not preferable. Overall, most of the positive torque was generated in the upstream which is the main power resource to the wind turbine. By combining torques generated by the blades, the total torque curve can be obtained and is shown in Figure IV-10 which is almost three times of the torque generated by one bladed H-rotor.

The model was applied to continue studying the aerodynamic performance of the H-rotor with three blades at different TSRs. The simulations were carried out at TSR=1, 1.5, 2, 2.5 and 3 which means the angular velocities of the moving mesh were set as ω =0.979rad, 1.468rad/s, 1.958rad/s, 2.447rad/s and 2.936rad/s. The H-rotor exhibited different aerodynamic performance at these TSRs in given fluid conditions. At the low TSRs, the generated power increased when the rotating speed increased. At a certain TSR, the maximum power coefficient ($C_{P\,max}$) could be achieved.
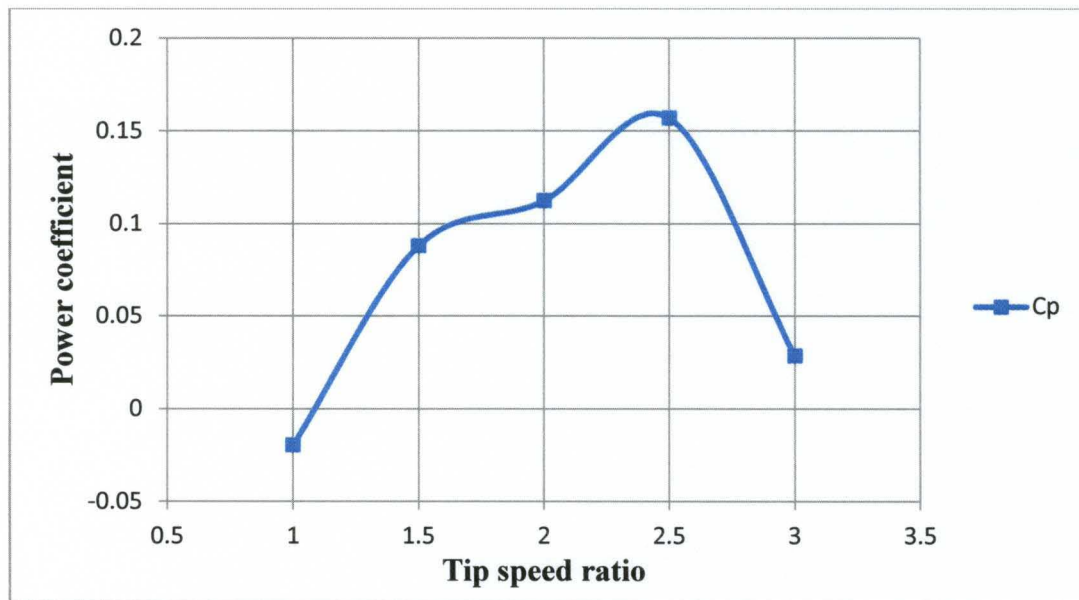
Figure IV-11 Power coefficients vs. TSR Curve with NACA 0015

Figure IV-11shows the power coefficients curve plotted against TSRs. The power output increased with TSRs. At around TSR=2.5, the best performance of H-rotor was achieved. After that, the aerodynamic performance showed a decreasing trend with the increase of the TSR. The turbine usually operated at around the maximum output TSR to transform the wind power as much as possible.

60

3. Comparison of turbine performance with different blade sections

The H-rotor with thicker airfoil blade section was carried out to investigate the performance. NACA0022 was used as the blade section in the simulation. In order to compare the performance of the blades, the tangential force coefficient curves were plot at TSR=1, 1.5, 2, 2.5 and 3.
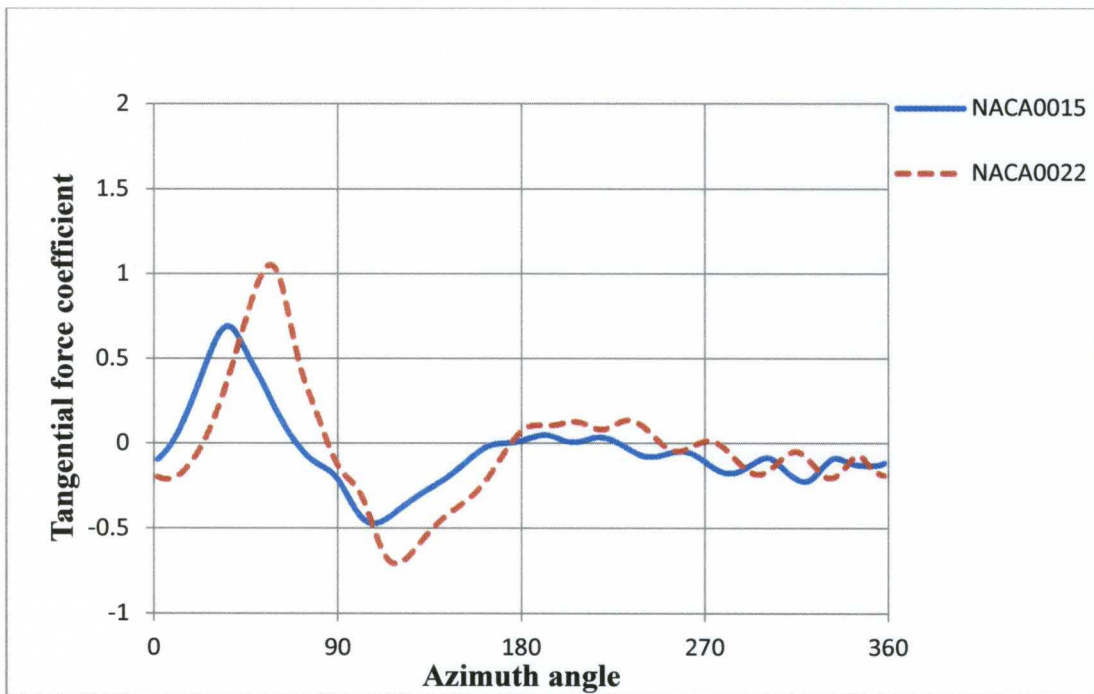
Figure IV-12 Tangential force coefficient against azimuth angle at TSR=1

Figure IV-13 Tangential force coefficient against azimuth angle at TSR=1.5

Figure IV-14 Tangential force coefficient against azimuth angle at TSR=2

Figure IV-15 Tangential force coefficient against azimuth angle at TSR=2.5

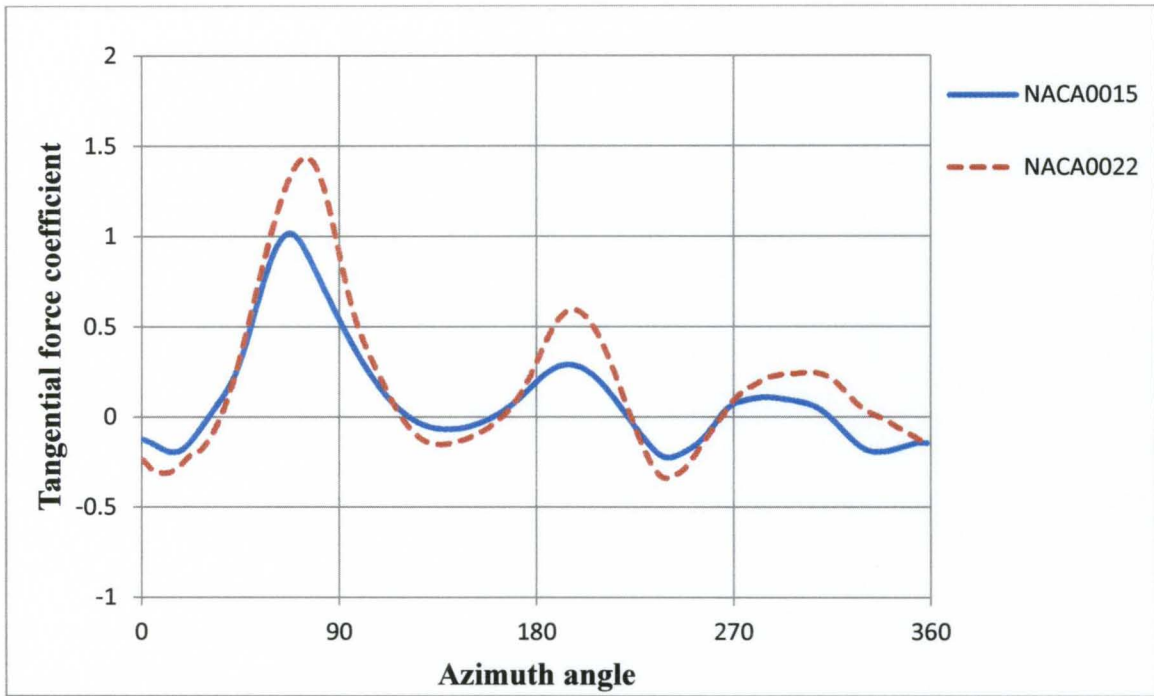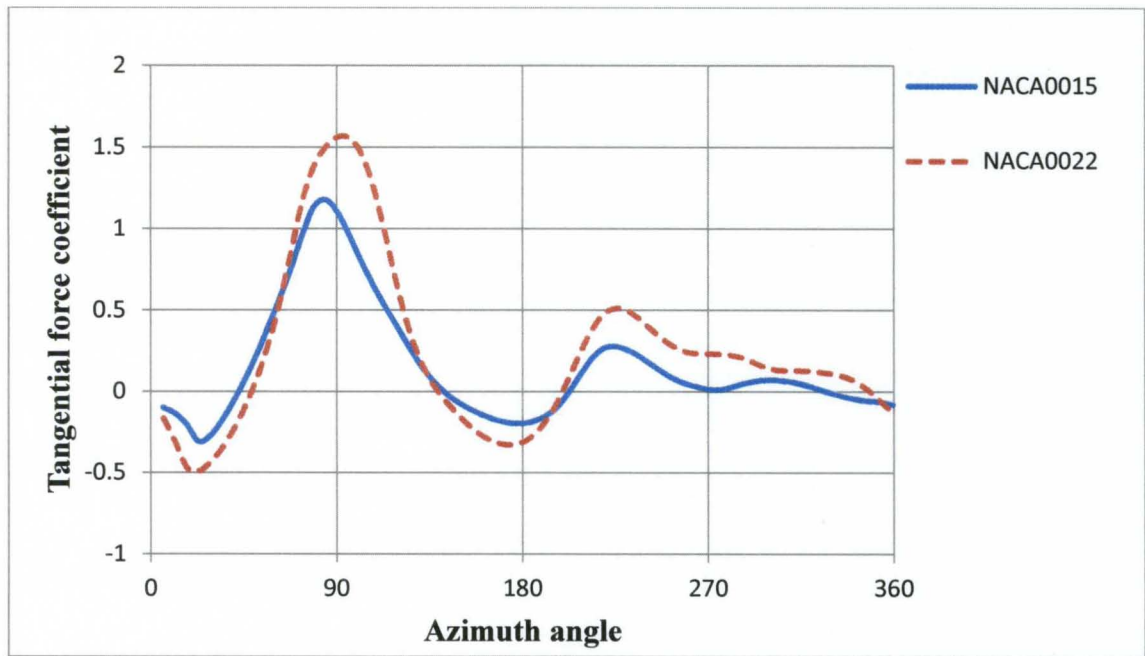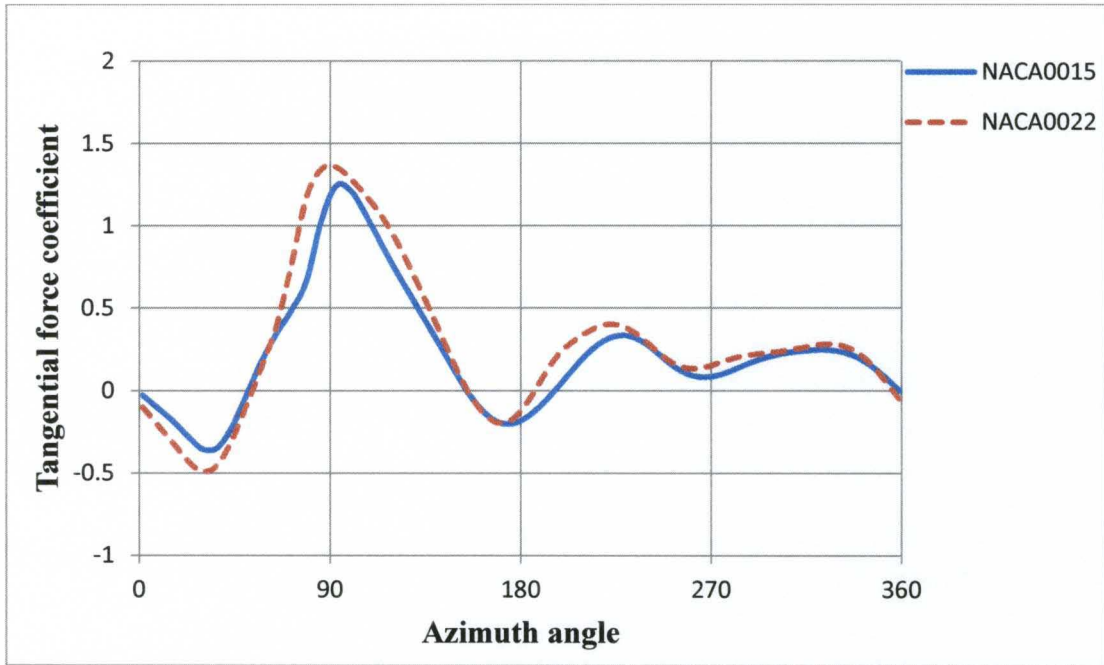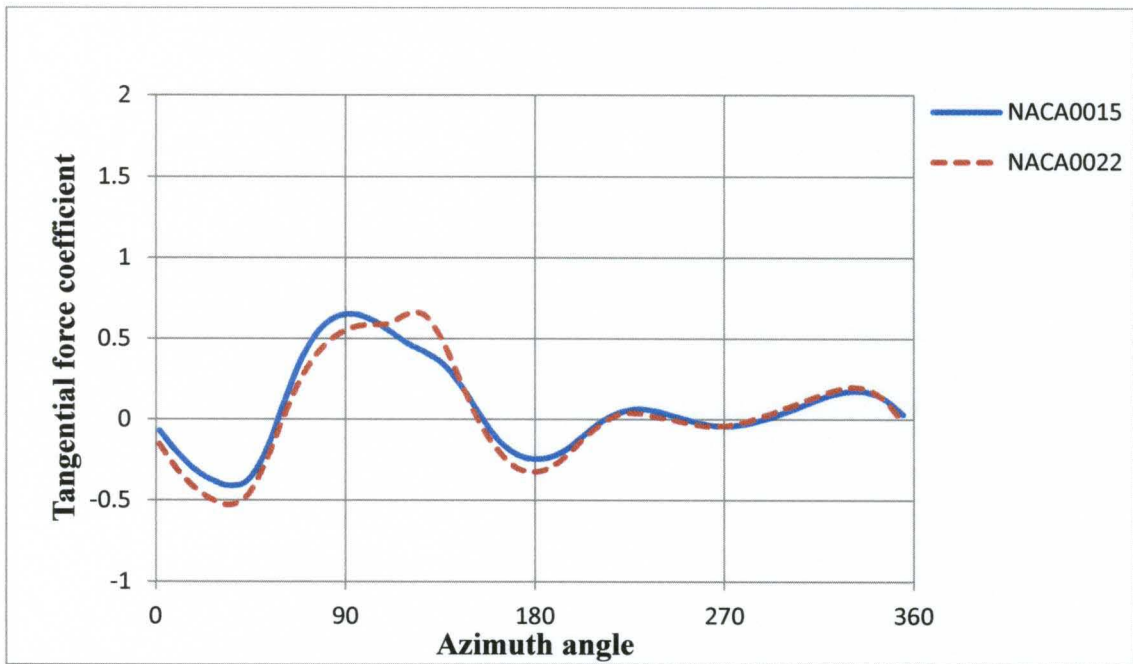**Figure IV-16 Tangential force coefficient against azimuth angle at TSR=3**

Healy (1978) has pointed out that thicker profiles are preferable for H-rotor when the Reynolds number was less than 2,000,000. Figure IV-12, Figure IV-13, Figure IV-14 and Figure IV-15 and Figure IV-16 exhibit the blade performances at different tip speeds. Due to the various angle of attack of airfoil, dynamic stall happened at low tip speed ratios. The dynamic stall is a non-linear unsteady aerodynamic effect that occurs when airfoils rapidly change the angle of attack. It showed that the NACA 0015 gave a better performance before the dynamic stall happened in the upstream. The dynamic stall happened more sudden and sharper than the NACA 0022 for the NACA 0015. Due to the large range of the angle of attack the dynamic stall was only observed at low tip speed ratios. From the graphs at low tip speed ratios, it was found that the tangential force of NACA 0015 was higher than NACA 0022 before dynamic stall happened. After dynamic stall happened, the tangential force of NACA 0022 increased more quickly than NACA 0015. The NACA 0022 gave a better performance after the dynamic stall. However, with the tip speed ratio increasing, the range of angle of attack became smaller and the dynamic stall didn't happen anymore. At the high tip speed ratios, the aerodynamic characteristics of airfoil before the dynamic stall became the determinant factor to the tangential force. NACA 0015 exhibited a better performance than NACA 0022.

Figure IV-17 showed the torque coefficient curves of different airfoil sections. The generating torque was highly improved with a thicker airfoil. When TSR=1, negative torque was generated with both NACA0015 and NACA 0022 which could lead to self-starting problems at low TSRs. A positive torque must be applied manually to help the turbine start rotating. Besides, though the power coefficient is negative for NACA0022, it improved slightly compared with NACA0015.

The power coefficient curves with different airfoil sections were plotted in Figure IV-18. It was found that the aerodynamic performance of H-rotor was improved significantly with NACA 0022. The maximum power coefficient was increased to 0.21 at around TSR=2.5 with NACA 0022. Though the performance of NACA 0022 was not better than NACA 0015's at high TSRs, it wouldn't cause any problem to wind turbines. Moreover, the NACA 0022 could decrease its own speed efficiently by itself when the blade is accelerated to high TSR at which structure problems might be caused. In general, NACA 0022 blades gave a better performance than NACA 0015 blades.
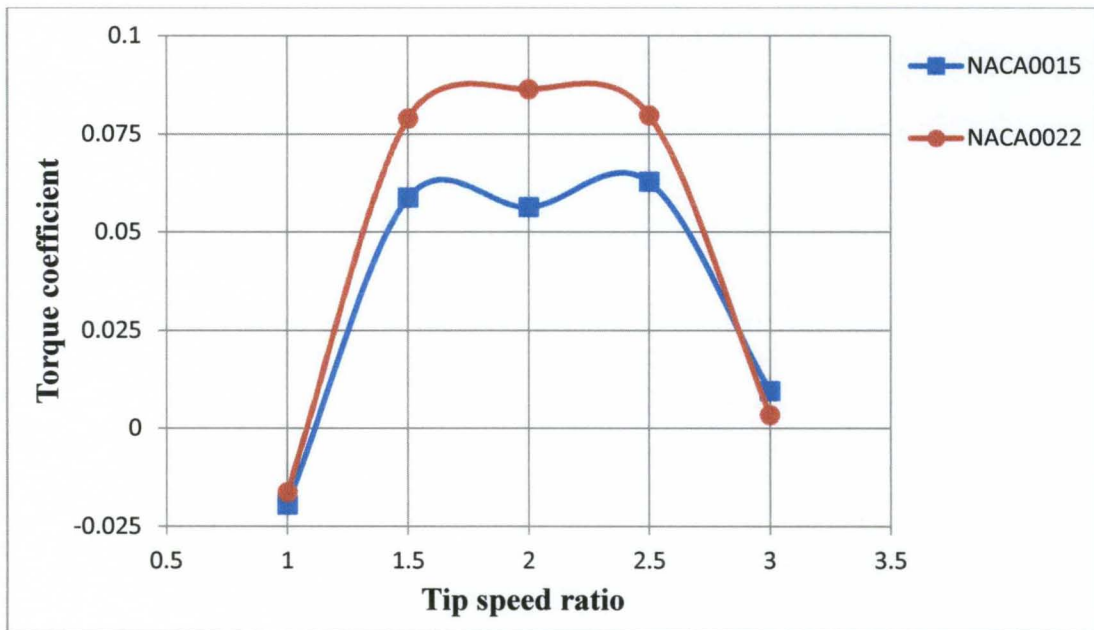
Figure IV-17 Comparison of torque coefficient curves with different airfoil sections
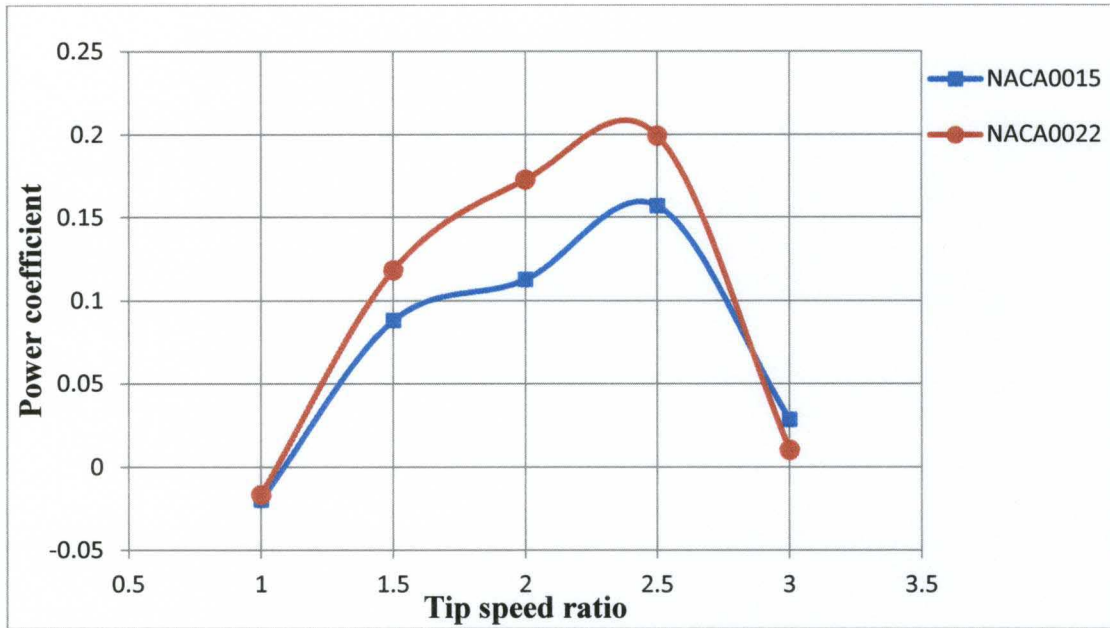
Figure IV-18 Comparison of power coefficient curves with different airfoil sections

These simulations were carried out at only $V_\infty = 3.9$ m/s, which was a quite low wind speed compared with other turbine operating conditions. The maximum power coefficient 0.21 is smaller than other turbines. However, this doesn't mean the performance of H-rotor is not efficient enough. The main reason is due to the low wind speed. The airfoil thickness influence has been studied by Healy (1978). It was shown that the maximum power coefficient is about 0.5 for H-rotor when the Reynolds number 2000,000 and higher maximum power coefficient could be achieved at higher Reynolds number.

V CONCLUSION

Numerical simulations were carried out to estimate the aerodynamic performance of H-rotors. The simple 2D simulations with only turbine blade cross sections were conducted by both Overture and Fluent. The DNS model and RNG $k - \varepsilon$ model have been applied to simulate the flow conditions individually.

1. The DNS model was applied to simulate the flow by solving incompressible time dependent Navier-Stokes equation directly with moving overlapping grid technique. The moving grids can easily handle the rotating motion of the airfoil. However, due to the limitation of computational and time resources, the DNS model could not describe the flow field accurately.

2. The transient RNG $k - \varepsilon$ turbulence model, using the modified incompressible Navier-Stokes equation was used to capture the aerodynamic performance of H-rotor. The sliding mesh technique was adopted to handle the motion of the blades. The turbulence model can predict the flow field precisely. The force coefficients obtained from the simulation show high level of agreement with the experimental data.

3. Different numbers of blades were applied on the H-rotor. The three bladed wind turbine presented a great improvement in producing power and was almost three times of the one bladed turbine. Most of the positive torque was generated in the

67

upstream where the rotor performance wasn't affected by the interactions between blades. As a result, almost three times of power generated by the one bladed H-rotor could be obtained by three bladed H-rotor.

4. H-rotors with two different blade sections were simulated by RNG $k - \varepsilon$ turbulence model. The H-rotors with NACA 0022 blade section exhibited better performance than with NACA 0015. Their maximum power coefficient was 0.21 at around TSR=2.5 for NACA 0015 while the maximum value obtained by NACA 0015 was 0.16 at the same TSR.

REFERENCES

1. *Users Guide Manual*, in *Fluent 12.0/12.1 Documentation*, 2009, Ansys Inc.

2. Allet, A. and I. Paraschivoiu, *Viscous Flow and Dynamic Stall Effects on Vertical-Axis Wind Turbines.* International Journal of Rotating Machinery, 1995. **2**(1): p. 1-14.

3. Association, W.W.E., *World Wind Energy Report 2010*, 2011.

4. Betz, A., *Introduction to the Theory of Flow Machines* 1966: Oxforder: Permago Press.

5. Bussel, G.J.W.v., et al., *Turby: concept and realization of a small VAWT for the built environment*, in *EAWE/EWEA conference*, April 2004: Delft.

6. Darrieus, G.J.M., U.S. Patent, Editor 1931.

7. El-Samanoudy, M., A.A.E. Ghorab, and S.Z. Youssef, *Effect of some design parameters on the performance of a Giromill vertical axis wind turbine.* Ain Shams Engineering Journal, 2010. **1**(1): p. 85-95.

8. Eriksson, S., Bernhoff, H., and Leijon, M., *Evaluation of different turbine concepts for wind power.* Renewable and Sustainable Energy Reviews, 2008. **12**(5): p. 1419-1434.

9. Guerrero, J., *Numerical Simulation of the Unsteady Aerodynamics of Flapping Flight*, in *Department of Civil, Environmental, Architectural Engineering*, 2009, University of Genoa.

10. Guerri, O., A. Sakout, and K. Bouhadef, *Simulations of the Fluid Flow around a rotating Vertical Axis Wind Turbine.* Wind Engineering, 2007. **31**(3): p. 149-163.

11. Gupta, R. and A. Biswas, *Computational fluid dynamics analysis of a twisted three-bladed H-Darrieus rotor.* Journal of Renewable and Sustainable Energy, 2010. **2**(4): p. 043111.

12.   Hamada, K., et al., *Unsteady flow simulation and dynamic stall around vertical axis wind turbine blades*, in *AIAA aerodynamics conference Reno,* 2008.

13.   Healy, J.V., *The Influence of Blade thickness on the Output of Vertical Axis Wind Turbines.* Wind Engineering, 1978. **2**(3): p. 146-155.

14.   Henshaw, W.D., Petersson, N. A., ed. *A split-step scheme for the incompressible Navier-Stokes equations.* Numerical Simulation of Incompressible Flows, ed. M. Hafez, World Scientific 2003. 108-205.

15.   Henshaw, W.D., *A fourth-order accurate method for the incompressible Navier-Stokes equations on overlapping grids.* Journal Name: Journal of Computational Physics; (United States); Journal Volume: 113:1, 1994: p. 13-25.

16.   Henshaw, W.D., *On Multigrid for Overlapping Grids.* Siam Journal on Scientific Computing, 2005. **26**(5): p. 1547-1572.

17.   Henshaw, W.D. and D.W. Schwendeman, *Moving overlapping grids with adaptive mesh refinement for high-speed reactive and non-reactive flow.* Journal of Computational Physics, 2006. **216**(2): p. 744-779.

18.   Hinze, J.O., *Turbulence.* Second Edition ed1975, New York: McGraw-Hill.

19.   Howell, R., et al., *Wind tunnel and numerical study of a small vertical axis wind turbine.* Renewable Energy, 2010. **35**(2): p. 412-422.

20.   Hwang, I.S., Y.H. Lee, and S.J. Kim, *Optimization of cycloidal water turbine and the performance improvement by individual blade control.* Applied Energy, 2009. **86**(9): p. 1532-1540.

21.   Iida, A., A. Mizuno, and K. Fukudome. *Numerical simulation of aerodynamic noise radiated form vertical axis wind turbines.* in *In: Proceedings of ICA2004, the 18th international congress on acoustics.* 2004. Kyoto, Japan.

22.   Klimas, P.C., *Airfoil treatments for vertical axis wind turbines*, 1985. p. Medium: X; Size: Pages: 7.

23.   Krohn, S., *Danish Wind Turbines: An Industrial Success Story*, 2002.

24.   Mertens, S., G. van Kuik, and G. van Bussel, *Performance of an H-Darrieus in the Skewed Flow on a Roof.* Journal of Solar Energy Engineering, 2003. **125**(4): p. 433-440.

25.   Morcos, V.H. and O.M.E. Abdel-Hafez, *Testing of an arrow-head vertical-axis wind turbine model.* Renewable Energy, 1996. **7**(3): p. 223-231.

26.   Muljadi, E., K. Pierce, and P. Migliore. *Control strategy for variable-speed, stall-regulated wind turbines*. in *American Control Conference, 1998. Proceedings of the 1998*. 1998.

27.   Musgrove, P.J., *Wind energy conversion: Recent progress and future prospects*. Solar & Wind Technology, 1987. **4**(1): p. 37-49.

28.   Noll, R.B. and N.D. Ham. *Analytical evaluation of the aerodynamic performance of a high-reliability vertical-axis wind turbine*. in *Proceedings of AWEA national conference*. 1980. USA.

29.   Oler, J.W., et al., *Dynamic stall regulation of the Darrieus turbine*, in *SANDIA REPORT*1983.

30.   Paraschivoiu, I., *Double-multiple streamtube model for darrieus wind turbines.* , in *Second DOE/NASA wind turbines dynamics workshop*1981: Cleveland, OH. p. 19-25.

31.   Paraschivoiu, I., *Double-Multiple Streamtube Model for Studying Vertical Axis Wind Turbines*. Jour. Propulsion, 1988: p. 370-377.

32.   Paraschivoiu, I., ed. *Wind turbine design: with emphasis on darrieus concept*. 2002, Polytechnic International Press.

33.   Paraschivoiu, I., et al., *Aerodynamic analysis of the Darrieus rotor including secondary effects*. J. Energy, 1983. **7**(5): p. 416-422.

34.   Paraschivoiu, I., O. Trifu, and F. Saeed, *H-Darrieus Wind Turbine with Blade Pitch Control*. International Journal of Rotating Machinery, 2009.

35.   Peace, S., *Another approach to wind (cover story)*. Mechanical Engineering-CIME, 2006. **126**(6): p. 28-31.

36.   Pezzinga, G., *Velocity Distribution in Compound Channel Flows by Numerical Modeling*. Journal of Hydraulic Engineering, 1994. **120**(10): p. 1176-1198.

37.   Riegler, H., *HAWT versus VAWT: Small VAWTs find a clear niche*. Refocus, 2003. **4**(4): p. 44-46.

38.   Shepherd, D.G., *Historical development of the windmill*, December, 1990, US Department of Energy: Washington, USA.

39.   Sim~ao Ferreira, C., G. van Bussel, and G. van Kuik, *2D CFD simulation of dynamic stall on a Vertical Axis Wind Turbine: verification and validation with PIV measurements*, in *45th AIAA Aerospace Sciences Meeting and Exhibit /ASME Wind Energy Symposium*2007.

40.   Staelens, Y., F. Saeed, and I. Paraschivoiu, *A Straight-Bladed Variable-Pitch VAWT Concept for Improved Power Generation.* ASME Conference Proceedings, 2003. **2003**(75944): p. 146-154.

41.   Strickland, J.H., *A performance prediction model for the darrieus turbine.*, in *International symposium on wind energy systems*1976: Cambridge, UK. p. C3-39-54.

42.   Strickland, J.H., B.T. Webster, and T. Nguyen, *A Vortex Model of the Darrieus Turbine: An Analytical and Experimental Study.* Journal of Fluids Engineering, 1979. **101**(4): p. 500-505.

43.   Takao, M., et al., *A straight-bladed vertical axis wind turbine with a directed guide vane row — Effect of guide vane geometry on the performance —.* Journal of Thermal Science, 2009. **18**(1): p. 54-57.

44.   Templin, R.J., *Aerodynamic performance theory for the NRC vertical-axis wind turbine*, in *NRC Lab. report*1974.

45.   Wilson, R.E., *Wind-turbine aerodynamics.* Journal of Wind Engineering and Industrial Aerodynamics, 1980. **5**(3-4): p. 357-372.

46.   Wilson, R.E. and P.B.S. Lissaman, *Applied aerodynamics of wind power machhines*, 1974, Oregon State University Corvallis.

47.   Yakhot, V., et al., *Development of turbulence models for shear flows by a double expansion technique.* Physics of Fluids A, 1992. **4**(7): p. 1510-1520.

APPENDIX

Nomenclature

λ = tip speed ratio

θ = azimuth angle

t = time

p = fluid pressure

ρ = fluid density

μ = dynamic viscosity

v = kinematic viscosity

$\vec{u}$ = velocity vector

u = X-component velocity

v = Y-component velocity

w = Z-component velocity

k = turbulence kinetic energy

ε = turbulence dissipation rate

F_{ta} = averaged tangential force in rotating period

F_t = tangential force

F_n = normal force

L = lift force per unit length

D = drag force per unit length

T = torque per unit length

P = aerodynamic turbine power output per unit length

C_L, C_D, C_t, C_n = lift coefficient, drag coefficient, tangential force coefficient, normal force coefficient

C_T = torque coefficient

C_P = rotor power coefficient

P_W = the available wind power in wind stream

V_∞ = free stream velocity

V_1 = wake velocity

V = induced velocity

a = the induced factor

W = relative wind speed

N = blade number

A = cross section area

ω = angular velocity

H = blade height

σ = solidity

Re = Reynolds number

α = angle of attack

CURRICULUM VITAE

YAN CHEN

EDUCATION:

08/2010 - Present   University of Louisville, Louisville, USA
(Expected)   Master of Science in Mechanical Engineering
                        GPA: 3.966/4.00

09/2005 – 07/2009   North China University of Water Conservancy
                        and Electric Power, Zhengzhou, China
                        Bachelor of Science
in Water Supply and Sewage Engineering
                        GPA: 82/100   Rank: 14/126

PROFESSIONAL EXPERIENCE:

08/2010—Present   University of Louisville, Louisville, USA
                        Research Assistant, Computational Fluid Dynamic Lab

02/2009—05/2009   HFUT Institute of Architectural Design, Shaoxing Branch,
                        Shaoxing, China
                        Full-time internship

09/2008—10/2008   Wulongkou Sewage Treatment Plant, Zhengzhou, China

HONORS &AWARDS:

Government Third-Class Scholarship (2008)
University Third-Class Scholarship (2007, 2008)
University Second-Class Scholarship (2006)